JGR Earth Surface

RESEARCH ARTICLE
10.1029/2023JF007098

Ablation-Limited Erosion Rates of Permafrost Riverbanks

Madison M. Douglas[1], Kimberly Litwin Miller[1], Maria N. Schmeer[1], and Michael P. Lamb[1]

[1]Division of Geological and Planetary Sciences, California Institute of Technology, Pasadena, CA, USA

Key Points:

- Flume experiments with frozen, erodible riverbanks were used to test and revise theory
- Erosion rates were affected by hydrodynamically rough banks that change the rate of heat transfer
- Ablation-limited bank erosion rates increase with warmer water and lower pore-ice content and are insensitive to bank temperature

Supporting Information:

Supporting Information may be found in the online version of this article.

Correspondence to:

M. M. Douglas,
mmdougla@caltech.edu

Citation:

Douglas, M. M., Miller, K. L., Schmeer, M. N., & Lamb, M. P. (2023). Ablation-limited erosion rates of permafrost riverbanks. *Journal of Geophysical Research: Earth Surface*, *128*, e2023JF007098. https://doi.org/10.1029/2023JF007098

Received 1 FEB 2023
Accepted 16 JUL 2023

Abstract Permafrost thaw is hypothesized to increase riverbank erosion rates, which threatens Arctic communities and infrastructure. However, existing erosion models have not been tested against controlled flume experiments with open-channel flow past an erodible, hydraulically rough permafrost bank. We conducted temperature-controlled flume experiments where turbulent water eroded laterally into riverbanks consisting of sand and pore ice. The experiments were designed to produce ablation-limited erosion such that any thawed sediment was quickly transported away from the bank. Bank erosion rates increased linearly with water temperature, decreased with pore ice content, and were insensitive to changes in bank temperature, consistent with theory. However, erosion rates were approximately a factor of three greater than expected. The heightened erosion rates were due to a greater coefficient of heat transfer from the turbulent water to the permafrost bank caused by bank grain roughness. A revised ablation-limited bank erosion model with a heat transfer coefficient that includes bank roughness matched our experimental results well. Results indicate that bank erosion along Arctic rivers can accelerate under scenarios of warming river water temperatures for cases where the cadence of bank erosion is set by pore-ice melting rather than sediment entrainment.

Plain Language Summary Many rivers in the Arctic have banks made up of permanently frozen sand and ice (permafrost) that are susceptible to erosion when they thaw. To understand how bank erosion may change as the Arctic climate warms, we conducted laboratory experiments using a channel with an erodible frozen bank. We found that warmer river water and lower bank-ice content produced faster erosion rates. In contrast, bank erosion was insensitive to the ground temperature. Bank erosion rates were three-fold faster than predicted by existing theory. We attribute the faster-than-expected erosion to a greater transfer of heat from the river water due to bank roughness. Our results imply that warming river water may increase riverbank erosion rates in permafrost regions, threatening communities and infrastructure built along Arctic rivers.

1. Introduction

Permafrost riverbank erosion threatens the homes, infrastructure, and livelihoods of people living in the Arctic (Hjort et al., 2018; Karjalainen et al., 2019). Permafrost regions contain 22% of the Earth's landmass (Obu, 2021; Obu et al., 2019) and ground temperatures are warming rapidly due to climate change (Biskaborn et al., 2019; Isaksen et al., 2016). These regions also contain major river systems which can erode their banks up to tens of meters per year (Rowland et al., 2019) (Figure 1). Hundreds of Alaskan communities experience a combined risk of bank erosion, permafrost thaw, and flooding (UAF & USACE, 2019), and it is uncertain how much these hazards will increase as the Arctic warms. Riverbank erosion has already caused some communities to relocate entirely (Bronen & Chapin, 2013; Maldonado et al., 2013), but studies disagree whether erosion rates will increase (Costard et al., 2014; Kokelj et al., 2013) or decrease (Ielpi et al., 2023) in response to climate change. Accurate mechanistic models of permafrost riverbank erosion are needed to predict bank erosion hazards and develop mitigation strategies.

Theory has been developed for permafrost riverbank erosion based on the one-dimensional Stefan solution (Costard et al., 2003; Randriamazaoro et al., 2007). In this scenario, the erosion rate is assumed to be ablation-limited, such that heat transfer and pore-ice melting set the erosion rate, and sediment is assumed to be immediately entrained following thaw (Figure 2). It is also possible that bank erosion is limited by sediment transport or slump blocks (Douglas, Dunne, & Lamb, 2023; Kanevskiy et al., 2016), but our focus here is to evaluate the ablation-limited end member. For ablation-limited erosion, bank erosion rates should depend on river flow velocity and water temperature because these parameters are the primary control on heat transfer from the river to the bank (Costard et al., 2003). Therefore, since Arctic rivers are experiencing increases in water temperature and discharge (Brabets & Walvoord, 2009; Liu et al., 2005; Peterson et al., 2002), riverbank erosion rates might significantly increase as the Arctic warms. The theory of Costard et al. (2003) for ablation-limited erosion

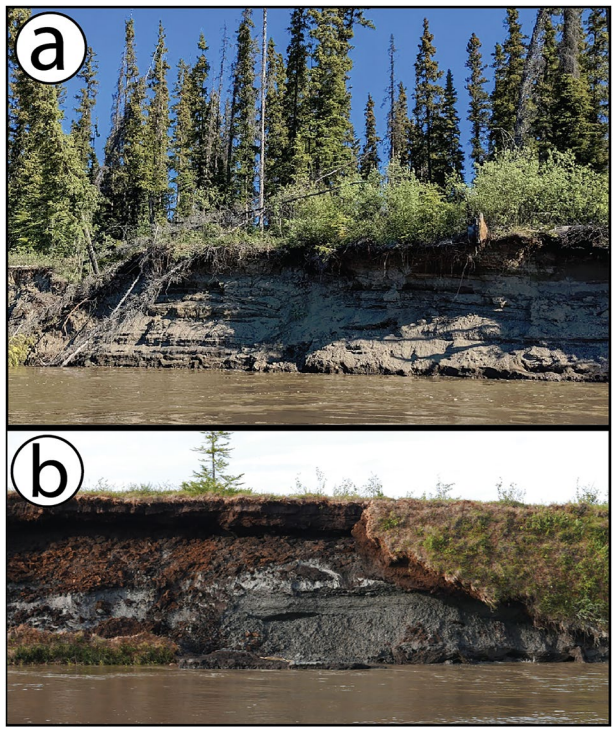

Figure 1. (a) Field photo of eroding permafrost sand and gravel riverbank along the Yukon River near Beaver, AK. The exposed bank is approximately 3 m tall. (b) Field photo of eroding permafrost silt and peat riverbank along the Koyukuk River near Huslia, AK. The exposed bank is approximately 1.5 m tall.

compares well to observed erosion of up to 40 m measured over 1–2 months for islands in the Lena River (Costard et al., 2014), but it over-predicts annual rates by hundreds of meters of erosion per year if applied over the entire open-water summer season. This partial disagreement between theory and observations motivates our investigation of ablation-limited erosion theory using flume experiments.

There have been few laboratory tests of permafrost bank erosion theory. The Costard et al. (2003) model used an empirical coefficient to parameterize heat transfer from the river water to the riverbank, based on experiments of flowing water over ice (Lunardini, 1986). However, it is unclear if the same heat transfer coefficient applies to a sediment bank with pore-ice, which is typical of permafrost floodplains. Other experiments measured erosion of a small block of frozen sand and ice that was inserted into a smooth-walled pressurized pipe or duct (Alexander, 2008; Costard et al., 2003; Dupeyrat et al., 2011). They found that higher water temperatures, greater water discharge, and lower permafrost ice content increased the erosion rate of the sample, consistent with theory. However, hydraulics are different in a pressurized duct compared to an open channel, and thaw rates in these experiments may have been affected by any protrusion of the sample into the pipe as well as the change in roughness from the hydrodynamically smooth pipe wall to the rough sample. For instance, the size, shape, spacing, and orientation of roughness elements are known to affect heat transfer by thinning and disrupting the thermally diffusive fluid sublayer (Miyake et al., 2001; Shishkina & Wagner, 2011; Yaglom & Kader, 1974).

Here, we present results from a permafrost river flume experiment designed to investigate the erosion rate of a hydraulically rough and erodible frozen riverbank under open-channel flow. First, we present existing theories for ablation-limited bank erosion and heat transfer from a turbulent fluid to a rough wall. Next, we show the experimental methods and results used to test the theories and evaluate the heat transfer coefficient. Finally, we discuss how the theory applies to natural rivers and the implications for Arctic riverbank erosion in a warming climate.

2. Theory for Permafrost Riverbank Erosion

2.1. Ablation-Limited Erosion Theory

Existing theory for permafrost riverbank erosion typically assumes ablation-limited conditions; that is, the erosion rate is set by the rate of bank thaw (Costard et al., 2003; Dupeyrat et al., 2011; Randriamazaoro et al., 2007). This is analogous to the theory developed for the geometry and evolution of subglacial and supraglacial channels, where the channel geometry is set by heat transfer between the flow and a pure ice boundary (Gulley et al., 2014; Karlstrom et al., 2013), but instead uses bank material properties that reflect a mixture of sediment and ice. Following Randriamazaoro et al. (2007), we derive the position of the thawing bank ($y = s$; m) and the bank temperature (T; °C) at a given time for the 1-D case (Figure 2a). The control volume consists of a thawing portion of a frozen riverbank with thickness ds (m) (Figure 2a). Following the conservation of heat,

$$\rho_b c_{p,b} \left.\frac{dT}{dt}\right|_{y=s} ds + q_f = q_w - q_r, \tag{1}$$

where q_f (J/m^2/s) is the latent heat flux into the bank, q_w (J/m^2/s) is the heat flux from the flowing river water to the bank, q_r (J/m^2/s) is the sensible heat flux conducted from the control volume to the frozen bank, ρ_b (kg/m^3) and $c_{p,b}$ (J/kg/°C) are the bulk density and specific heat of the bank material, and y is the coordinate normal to the bank. Equation 1 assumes a 1-D heat budget where the only heat source is water flowing past the bank. This assumption is supported by field observations that flowing water cuts deep thermoerosional niches and creates characteristic overhangs in permafrost riverbanks, implying that the heat flux from the air is a relatively minor

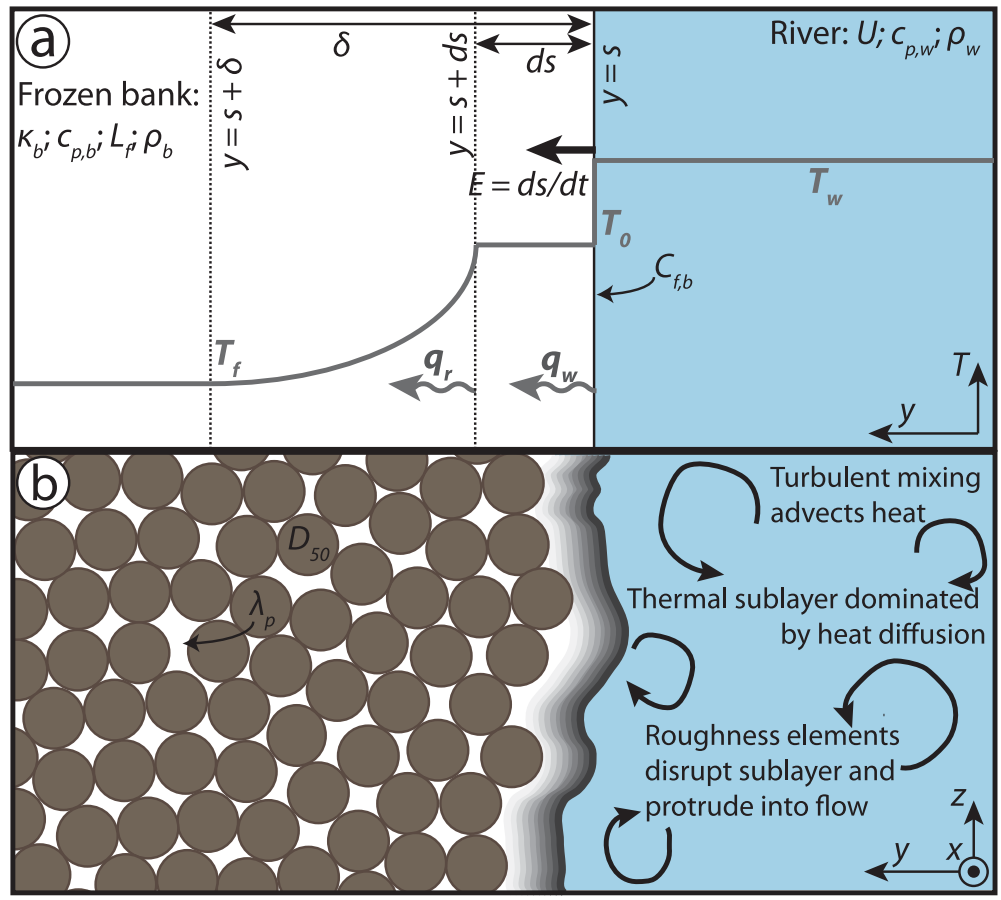

Figure 2. 1-D model for permafrost bank erosion ($E = ds/dt$, m/s) by ablation. (a) Schematic 1-D cross-section showing a temperature profile (T) into a bank (y-direction) with the river flowing into the page. The erosion model considers heat fluxes from the flowing water to the bank (q_w, J/m^2/s) in a control volume of width ds (m). Heat flux from the river depends on water flow velocity (U, m/s), temperature (T_w, °C), density (ρ_w, kg/m^3), specific heat capacity ($c_{p,w}$, J/kg/°C), and the bank coefficient of friction ($C_{f,b}$, dimensionless). The permafrost bank has a constant thermal conductivity (κ_b, W/m/°C), specific heat capacity ($c_{p,b}$, J/kg/°C), latent heat of fusion (L_f, J/kg), and bulk density (ρ_b, kg/m^3). The bank temperature in the control volume is at the temperature of fusion (T_f, °C) and decreases to the background temperature (T_0, °C) over a distance δ (m) driven by conduction (q_r, J/m^2/s). (b) Cartoon cross-section of the bank showing how roughness affects heat transfer from a fully turbulent fluid (flowing out of the page) to a hydraulically rough wall. The bank has median grain size D_{50} (m) and volumetric ice content λ_p (m^3/m^3). Far from the wall, heat transfer is dominated by heat advection in turbulent eddies, while heat transfer near the bank occurs by molecular diffusion through a thin sublayer. Roughness elements cause more rapid heat transfer to the bank by thinning or protruding through the diffusive sublayer.

component of bank erosion (Walker & Hudson, 2003). Bank material properties are assumed to be spatially and temporally homogeneous, so that ρ_b and $c_{p,b}$ are constants.

A thawing bank should be at the melting temperature, such that $T|_{y=s} = T_f$, where T_f (°C) is the temperature of fusion of pore ice; thus, in Equation 1, $\frac{dT}{dt}\Big|_{y=s} = 0$. In addition, the heat flux due to fusion is

$$q_f = \rho_b L_f \frac{ds}{dt}, \tag{2}$$

where L_f (J/kg) is the latent heat of fusion of the frozen bank. Substituting these expressions into Equation 1 and rearranging results in

$$\rho_b L_f \frac{ds}{dt} = q_w - q_r. \tag{3}$$

To evaluate q_r in Equation 3, heat flow is modeled by conduction within the frozen bank (i.e., where $y \geq s$), such that

$$-\rho_b c_{p,b} \frac{\partial T}{\partial t} = \frac{\partial q}{\partial y}, \tag{4}$$

with q as the heat flux (J/m^2/s) within the frozen bank. Heat conduction occurs from $y = s$ to $y = s + \delta$, and beyond $y = s + \delta$ the bank temperature is set to a constant background value T_0 (°C) (Costard et al., 2003). Integrating Equation 4 from $y = s$ to $y = s + \delta$ and using the chain rule results in the following equation:

$$\rho_b c_{p,b} \int_s^{s+\delta} \frac{\partial T}{\partial y} \frac{\partial y}{\partial t} dy = \int_s^{s+\delta} \frac{\partial q}{\partial y} dy. \tag{5}$$

As the bank erodes, δ (m) is assumed to remain constant, so the thermal gradient within the bank translates in the y-direction at the rate of bank erosion; thus, $dy/dt = ds/dt$. Then, Equation 5 can be solved and rearranged using the boundary conditions $T(t, y = s + \delta) = T_0$, $T(t, y = s) = T_f$, $q(t, y = s + \delta) = 0$, and $q(t, y = s) = q_r$, to find,

$$q_r = \rho_b c_{p,b} \frac{ds}{dt} (T_f - T_0). \tag{6}$$

The latent heat of fusion in Equations 2 and 3 for a saturated sand-ice mixture (Dupeyrat et al., 2011) depends on the mass fraction of ice in the bank (f_{ice}; kg ice/kg frozen bank) and the latent heat of fusion of ice ($L_{f,\text{ice}}$; J/kg):

$$L_f = f_{\text{ice}} L_{f,\text{ice}}. \tag{7}$$

The specific heat of the bank ($c_{p,b}$) is calculated as a sum of the specific heat of ice ($c_{p,\text{ice}}$; J/kg/°C) and the specific heat of quartz sand ($c_{p,s}$; J/kg/°C), weighted by the mass fraction of ice:

$$c_{p,b} = f_{\text{ice}} c_{p,\text{ice}} + (1 - f_{\text{ice}}) c_{p,s}. \tag{8}$$

Typically, the latent heat of fusion for ice is orders of magnitude greater than its specific heat, so we expect that the phase change and not the permafrost temperature should set the rate of pore-ice thaw.

The heat transfer from a turbulent fluid to a wall depends on fluid velocity, U (m/s), and an empirical coefficient that describes the efficiency of heat transfer (Nield & Bejan, 2017). Thus, q_w in Equation 3 can be written as,

$$q_w = C_h \rho_w c_{p,w} U (T_w - T_b), \tag{9}$$

where C_h (dimensionless) is the heat transfer coefficient, ρ_w (kg/m^3) is water density, $c_{p,w}$ (J/kg/°C) is the specific heat of water, T_b (°C) is the bank temperature, and T_w (°C) is the water temperature. In the transient solution, T_b may change in response to q_w, but the ablation-limited solution given by Equation 3 requires $T_b = T_f$.

The final expression is found from substituting Equation 6 for q_r in Equation 3, Equation 9 for q_w in Equation 3, and using Equations 7 and 8 to account for the fraction of pore ice (f_{ice}) in the latent heat of fusion and heat capacity. Solving for the bank erosion rate $E \equiv \frac{ds}{dt}$ for the 1-D ablation-limited case results in Randriamazaoro et al. (2007):

$$E = \frac{C_h \rho_w c_{p,w} U (T_w - T_f)}{\rho_b (f_{\text{ice}} L_{f,\text{ice}} + (f_{\text{ice}} c_{p,\text{ice}} + (1 - f_{\text{ice}}) c_{p,s})(T_f - T_0))}. \tag{10}$$

2.2. Heat Flux Parameterizations

Applying Equation 10 requires specifying the heat transfer coefficient C_h. Different empirical relations have been proposed for C_h. Costard et al. (2003) and Dupeyrat et al. (2011) calibrated C_h based on a series of frozen flume experiments to evaluate the rate of heat transfer from the water to a frozen bank. Both coefficients were calculated as a function of the thermal conductivity of water (κ_w; J/m/s/°C), the Prandtl number (Pr), and the Reynolds number (Re), using flow depth as the characteristic length scale:

$$C_h = A \kappa_w \text{Pr}^{\alpha} \text{Re}^{\beta} / (\rho_w c_{p,w} U H). \tag{11}$$

The Prandtl number ($\text{Pr} = \rho c_{p,w} \nu / \kappa_w$) represents the dimensionless ratio of momentum diffusivity over thermal diffusivity and depends on the fluid kinematic viscosity (ν; m^2/s). The Reynolds number is the non-dimensional

ratio of fluid inertial forces over viscous forces, with Re = UH/ν. For application to natural rivers, Costard et al. (2003) used values of $A = 0.0078$, $\alpha = 0.3333$, and $\beta = 0.9270$ constrained from flume experiments of water flowing over pure ice (Costard et al., 2003; Lunardini, 1986). During these experiments, the ablating ice developed scallops on the scale of tens of centimeters, so heat transfer may have been influenced by form drag from the scallops (Lunardini, 1986). In this case, $\beta \sim 1$, so C_h is mostly independent of flow velocity (in Equation 11, $\mathrm{Re}/UH \sim 1/\nu$).

Yaglom and Kader (1974) proposed an alternative formulation for C_h that explicitly considers how wall roughness affects heat transfer. They used the Reynolds analogy and asymptotic mapping of the advective and diffusive thermal sublayers analogous to the derivation of the log law (Figure 2b). Their formulation has been extensively used in sea-ice models (Malyarenko et al., 2020) but has not been applied previously to permafrost riverbanks. Assumptions in their theory include a negligible longitudinal pressure gradient and homogeneous wall roughness. They used linear interpolation to find a solution that includes hydrodynamically rough flow (roughness Reynolds number $\mathrm{Re}_{k_s} = k_s u^*/\nu > 100$, with $u^* = U\sqrt{C_{f,b}}$) as well as hydrodynamically smooth flow. These are reasonable assumptions for permafrost rivers, which are fully typically turbulent with hydraulically rough banks due to coarse sand and gravel grains and morphological roughness elements such as slump blocks and vegetation (Figure 1). Their final expression when integrated over the flow field is Yaglom and Kader (1974); their Equations 22 and 23:

$$C_h = \frac{\sqrt{C_{f,b}}}{-\alpha \ln \eta_1 + \beta_1 + \beta_t}. \tag{12}$$

C_h depends on the bank coefficient of friction ($C_{f,b}$; dimensionless), the relative roughness element height ($\eta_1 = k_s/H$; dimensionless), the von Kármán constant ($\kappa = 0.41$), and empirical constants from the law of the wall ($\alpha = 2.12$; $\beta_1 = 0.5$). For hydraulically rough flows ($\mathrm{Re}_{ks} > 100$), $\beta_t = \beta_r$, with $\beta_r = \sqrt{\mathrm{Re}_{k_s}}\left(b_1 \mathrm{Pr}^{\frac{2}{3}} - b_2\right)$. For smooth to transitional flow ($\mathrm{Re}_{ks} \leq 100$), $\beta_t = \beta_r(\mathrm{Re}_{ks}/100) + \beta_s(1 - Re_{ks}/100)$, where $\beta_s = 12.5\mathrm{Pr}^{2/3} - 6$. Next, we describe the experimental approach and methods to test the bank erosion model (Equation 10) and the two different relations for the heat transfer coefficient (Equations 11 and 12).

3. Methods

3.1. Experimental Goals and Approach

The goal of our frozen flume experiments was to evaluate the relations for the heat transfer coefficient for conditions similar to permafrost rivers. We simulated ablation-limited permafrost riverbank erosion, where permafrost was directly in contact with the flowing river water. The experiments were not intended to be scale models of any specific river, but we did consider important dimensionless numbers so that the experiments had similar thermal and hydraulic states as natural permafrost rivers. The experiments were conducted under fully turbulent ($\mathrm{Re} \sim 10^5$) and subcritical (Froude number < 1) flow with hydraulically rough bed ($\mathrm{Re}_{k_s} > 100$) and an eroding bank in the transitional roughness regime (Table 1). We also scaled our flume experiments to the thermal regimes of natural permafrost rivers. We used the Biot number to compare heat transfer to the bank versus conduction within the bank ($\mathrm{Bi} = C_h \rho_w c_{p,w} UH/\kappa_b$), where κ_b is the bank thermal conductivity (W/m/°C), and the Stefan number to compare heat transfer to the bank ($\mathrm{St} = c_{p,w}(T_w - T_f)/H$). Using calculated values for bank thermal conductivity and best-fit model results for C_h (see Section 4.2), we find Bi ~ 0.10 and St ~ 130–660. For comparison, we estimated similar values (Bi ~ 0.40 and St ~ 8–80) from field measurements of the gravel-bedded Atigun River, Alaska, using data from Scott (1978).

We conducted five experiments to vary water temperature, bank temperature, and mass fraction of water ice while holding the other variables approximately constant. The effect of water temperature was evaluated by comparing Experiments 1–3; bank temperature was evaluated by comparing Experiments 3 and 4; and pore-ice fraction was evaluated by comparing Experiments 2 and 5 (Table 2).

3.2. Experimental Methods

The experiments were designed to simulate a straight half-width channel by using one fixed hydrodynamically smooth wall and one erodible permafrost bank in the Caltech Earth Surface Dynamics Laboratory (Figure 3).

Table 1
Experimental Hydraulic Conditions for All Frozen Banks

Variable	Symbol	Units	Values
Bank median grain size	$D_{50,bank}$	m	0.00026132
Bank 84th percentile grain size	$D_{84,bank}$	m	0.00036361
Bed median grain size	$D_{50,bed}$	m	0.019
Bed 84th percentile grain size	$D_{84,bed}$	m	0.021
Water discharge	Q_w	m^3/s	0.00221–0.00756
Channel depth	H	m	0.056
Channel width	B	m	~0.10–0.30
Average water flow velocity	U	m/s	~0.6–0.7
Water Reynolds number	Re	Dimensionless	$\sim 3.04 \times 10^5$
Bank roughness Reynolds number	Re_{k_s}	Dimensionless	~90
Water Froude number	Fr	Dimensionless	~0.83
Prandtl number	Pr	Dimensionless	10
Stefan number	St	Dimensionless	~130–660
Biot number	Bi	Dimensionless	~0.10

Note. Water discharge and channel width were increased throughout each experiment as the channel widened.

We placed the channel along the smooth wall, rather than in the middle of the flume, to suppress meandering or braiding. The smooth plexiglass wall had minimal friction relative to the rough bed and sediment bank, and therefore the half-width experiment can be considered representative of a full-width channel with two sediment banks that is twice as wide (Pitlick et al., 2013).

The flume was 0.75 wide and 7.60 m long, ending in a reservoir filled with chilled water. We evaluated bank erosion within a test section 0.70 m long centered in a 1.8 m reach bound by the clear plexiglass wall of the flume on river right and an erodible bank consisting of a frozen mixture of sand and ice on river left. The bankfull channel was initially set to 0.056 depth and 0.10 m width for each experiment. During the experiment, the channel width increased due to bank erosion to a final value of about 0.3 m. We increased water discharge to maintain a constant water depth as bank erosion progressed and the channel widened and used a backwater model (see Text S3 in Supporting Information S1) to account for variations in channel hydrodynamics throughout the experiment.

We controlled water temperature and bank temperature using a Mokon AL Iceman chiller. The chiller recirculated a 30% mixture of glycol in water through flexible pipes and mats arranged in the end tank and end barrels to chill the water, and in the channel under the bed material and on the river-left flume wall to freeze the bank material (Figure 3). The experiments were not conducted in a climate-controlled room, so air temperature was variable.

We constructed the frozen, erodible bank and floodplain in layers to make a uniform mixture of sand ($D_{16} = 0.16198$, $D_{50} = 0.26132$, and $D_{84} = 0.36361$ mm; Figure S1 in Supporting Information S1) and pore ice.

Table 2
Frozen Bank Properties for Each Experiment, With Variability Reported as 1 Standard Deviation

Experiment	Bed slope (m/m)	Water temperature (°C)	Bank temperature (°C)	Fraction ice (wt%)	Bulk density (g/cm^3)	Measurement time interval (stage 1) (min:sec)	Bank erosion rate (mm/s)
Experiment 1	0.0156	1.9 ± 0.1	−5.8 ± 0.7	33.0 ± 0.5	1.54 ± 0.04	40:06	0.075 ± 0.032
Experiment 2	0.0144	6.9 ± 1.5	−4.1 ± 0.8	23.6 ± 1.1	1.57 ± 0.06	19:32	0.16 ± 0.07
Experiment 3	0.0249	8.8 ± 0.6	−4.4 ± 0.7	27.7 ± 5.7	1.71 ± 0.09	6:52	0.26 ± 0.06
Experiment 4	0.0149	6.3 ± 1.0	−7.1 ± 0.6	21.4 ± 0.5	1.65 ± 0.36	15:00	0.19 ± 0.06
Experiment 5	0.0205	6.2 ± 0.2	−8.2 ± 0.9	31.3 ± 2.9	2.05 ± 0.16	5:46	0.23 ± 0.03

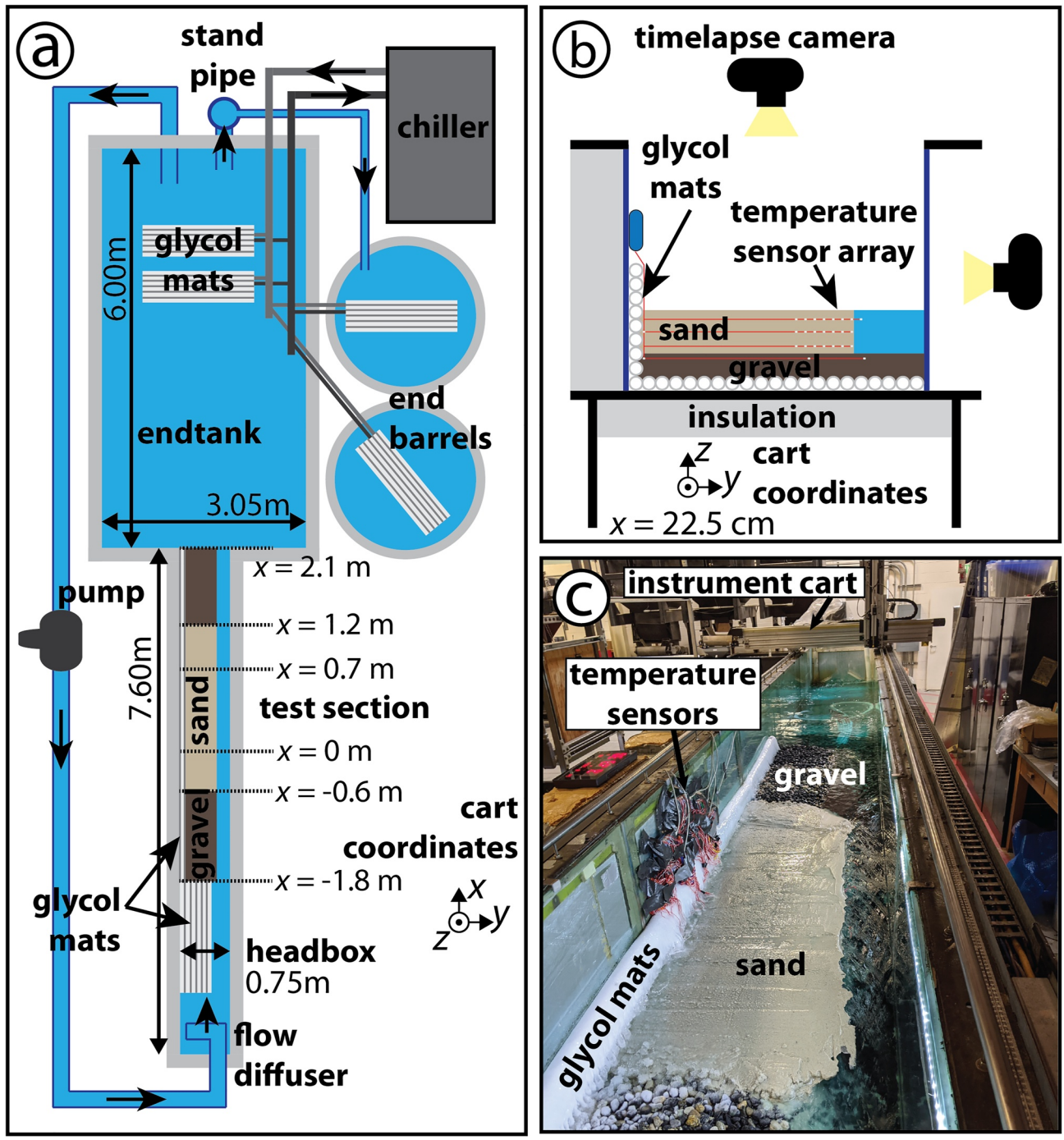

Figure 3. Frozen channel experimental setup in Caltech Earth Surface Dynamics Laboratory. (a) Top-down cartoon of the flume setup. Glycol was cooled by the chiller and circulated through a set of flexible pipes and mats to freeze the bank and cool the water in the end tank. Water was circulated by the pump from the end tank through the flow diffuser and into the experiment headbox, where it flowed past gravel and sand. Overflow of the stand-pipe went into external barrels. (b) Side-looking cartoon of the flume test section. Glycol mats line the side and base of the flume, and the exterior of the flume was covered by insulation. An array of temperature sensors was frozen into the eroding, sandy bank, and we recorded 10-s timelapse imagery using down- and side-looking cameras. (c) Photograph during a flume experiment. The glycol mats and temperature sensors are visible protruding up past the bank. The instrument cart ran on rails (visible in the lower right foreground) and carried a laser to measure topography as well as a sonar to measure water slope throughout the experiments.

We used a 0.1 m wide mold along the length of the sandy bank to form the initial channel on river right. We filled the region between the mold and the river-left flume wall with the sand-water mixture and placed it on top of a graded gravel bed. We built the bank material by laying ∼1.5 cm thick layers of saturated sand, graded each layer to parallel the bed slope, and then covered it with insulation to freeze overnight. Temperature sensors

(Minco S667PFZ40BC resistance temperature detectors with ±0.2°C resolution) were placed in the bank material before stacking the next layer. Three arrays of sensors in the bank were located in upstream (x = 2.5 cm), middle (x = 22.5 cm), and downstream (x = 42.5 cm) locations extending perpendicular to the channel (in the y-direction). The upstream and downstream arrays consisted of one line of sensors spaced 3 cm apart at an elevation above the thalweg of $z \sim 3$ cm. The middle array consisted of three lines of sensors with similar spacing in the y-direction at $z \sim 1$, 3, and 5 cm plus additional sensors at the base of the bank ($z = 0$ cm) and near the frozen wall ($y = 67.5$ cm). Finally, a temperature sensor was placed protruding into the channel to measure water temperature at $z \sim 5$ cm at each sensor array x-coordinate.

The channel bed was composed of gravel (D_{16} = 18, D_{50} = 19, and D_{84} = 21 mm; Figure S1 in Supporting Information S1), and the same gravel was used as river-left bank material for 1.2 m upstream and 0.9 m downstream of the sand-banked section. The gravel banks prevented erosion near channel headbox or outlet and helped to condition the flow and reduce spatial accelerations as it entered and exited the test section. The experiments were designed such that the gravel was below the threshold of motion. The gravel-banked reaches had a bankfull depth identical to the test section (0.056 m) and a bankfull width of 0.25 m. The gravel bed in the test section was graded by hand to a slope that ranged from 1.5% to 2.5% in different experiments (Table 2). Some pore ice formed in the gravel reaches, but the large pore spaces made the gravel drain relatively efficiently. The gravel banks maintained an angle of ~25°, slightly below the angle of repose.

We sampled the sandy bank material using a chisel and calculated the bulk density (ρ_b) and mass fraction of ice (f_{ice}) for each experiment (Table 1). We obtained the volume of the samples by differencing 1 × 1 mm gridded laser elevation scans with vertical accuracy of ~10 microns, before and after sampling. The samples were weighed before and after oven drying at 70°C to find the mass of sand and ice (Table 2).

To calibrate the temperature sensors, we submerged them in an ice water bath at 0°C for multiple hours. Each sensor showed little temperature variation, typically giving a Standard Deviation (SD) of less than 0.1°C, which was smaller than the reported precision of ±0.2°C. However, some sensors showed offset from 0°C. Therefore, we took the mean temperature of each sensor and subtracted that from the sensor with the lowest SD whose mean temperature was closest to 0°C. We used this correction offset while processing data for all experiments.

Temperature data were recorded using MicroDAQ data acquisition cards at 2 Hz. The initial bank temperature (T_0) was found by taking the mean ± 1 SD of the middle layer of the middle section bank temperatures for 5 min before the experiment started. The mean ± 1 SD of the water temperature was measured at the middle section during the period of uniform bank erosion when we calculate erosion rates. For subsequent analyses, we used a 10-s (20-measurement) smoothing window to average the temperature data over a similar interval to our timelapse imagery.

Water discharge was recorded every 10 s using an in-line flowmeter and controlled during each experiment using a variable frequency drive. We accounted for the time delay between the discharge at the flow meter and the discharge in the test section. We calibrated the water discharge by taking the time to fill a 5-gal container (n = 4–6) at 4 different discharges. We calculated uncertainty by making a linear fit to 1 SD of the measured discharge versus the flowmeter. This uncertainty was propagated through subsequent calculations.

To measure the evolving channel width during the experiment, we took overhead photographs (Nikon D750, 300 dpi resolution) every 10 s synchronized using DigiCamControl (Figure 4; Movies S1, S2, S3, S4, and S5). The water was dyed blue to enhance the contrast between the flowing water and eroding bank. Images were corrected for distortion using grids surveyed with the cart to ~0.1 mm precision using Adobe Photoshop CS4 (Figure 4b). The blue band was used to isolate the water and bank material using the Matlab v2020a image processing package (Figure 4c; Table S1 in Supporting Information S1). Images were cropped to isolate the test section and exclude portions of the bank that formed overhangs during each experiment. Incorrect classification of the bank material (e.g., from exposed temperature sensors or glint) was eliminated using the Matlab function imfill.m (Figure 4d) and by eye (Figure 4e). We summed the wetted top area of the channel, A_T (m^2), and then used this measurement to find the average bank erosion rate (m/s) as

$$\overline{E} = \frac{\Delta A_T}{L \Delta t}, \tag{13}$$

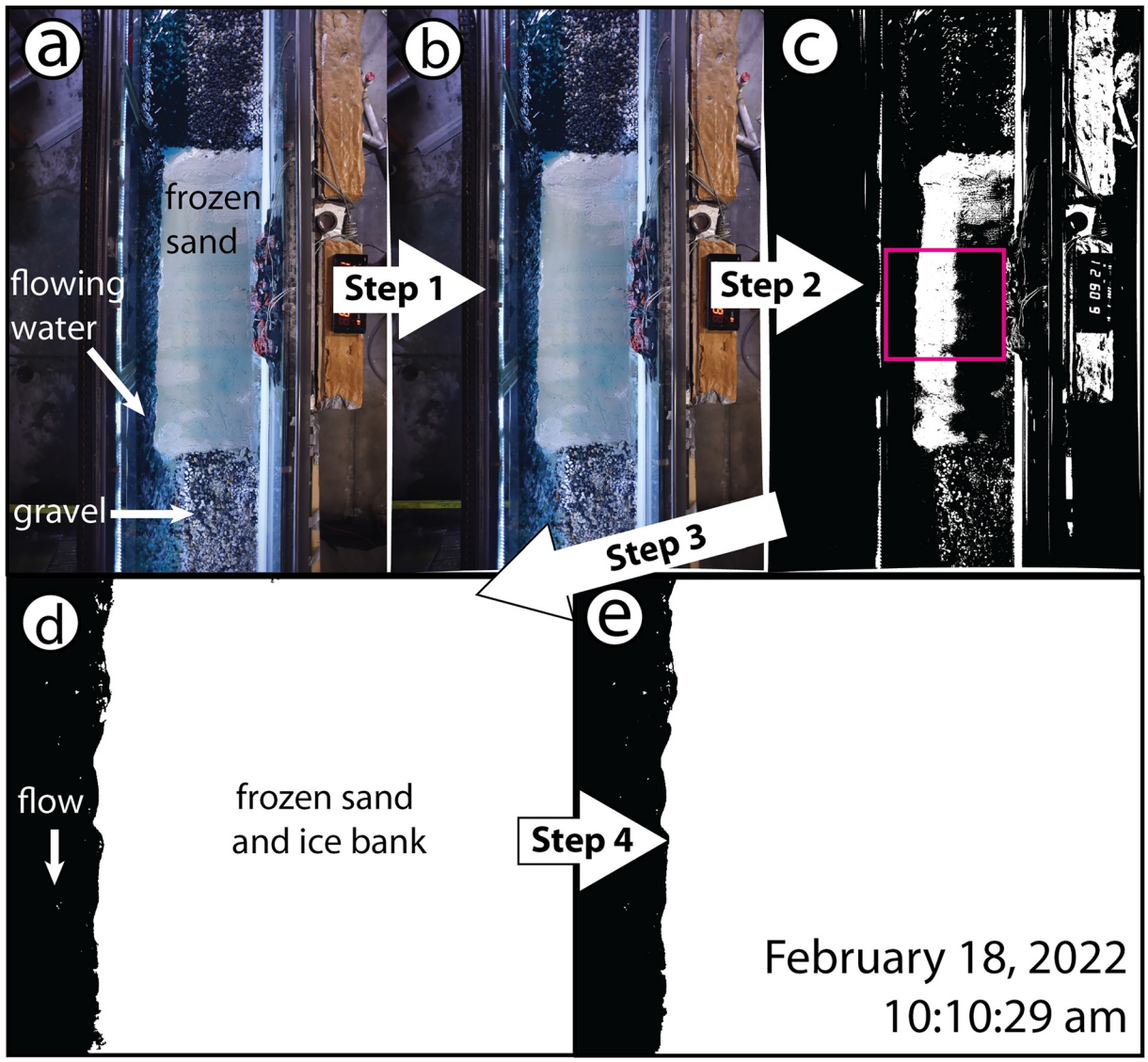

Figure 4. Steps for image processing to extract channel width and bank erosion rates. (a) Original image from overhead, down-looking camera. Blue dyed water flows from the top to the bottom of the image. (b) The image is corrected for camera lens distortion so that the pixels are at known values of the carriage coordinates. (c) Thresholded red band of the .jpg image, with light pixels considered part of the eroding bank. (d) The thresholded image is clipped to the test section (70 cm channel length, outlined in pink in panel (c)) and the interior of the bank top is filled in. (e) The image is reviewed and small artifacts are manually removed.

where the test section length is $L = 0.70$ m. The timelapse had $\Delta t = 10$ s, and erosion rates were smoothed using a moving average with 1-min window size and 1 SD uncertainty (Figure 6).

We also used the channel-width, flow discharge, and flow depth measurements to calculate the cross-sectionally averaged flow velocity (U). We used mass balance (Figure 3d) such that $Q_w = A_{xs}U$, where A_{xs} (m^2) is the channel cross-sectional area. We estimated $A_{xs} = CHB$, where $B = A_T/L$ is the channel top width (m), and C is a correction factor to account for any deviation in cross-section shape from rectangular. Using the topographic scans of the channel topography when dry confirmed that $C \sim 1$ within 5% uncertainty, which we used for all the experiments.

To calculate the friction coefficient on the eroding wall, we linearly partitioned the total frictional stress between components for the gravel bed, smooth flume wall, and grain and formed drag on the eroding frozen bank using the approach of Vanoni and Brooks (1957). For the smooth flume wall, we evaluated the skin friction coefficient using Blasius (1950). To find the friction coefficient corresponding to the immobile gravel, we conducted a series

of additional experiments where the entire river-left bank of the test section was composed of immobile gravel rather than frozen sand (Text S2.1 in Supporting Information S1). For these gravel-banked experiments, we fit the 1-D backwater equation to measured water surface data to find the total frictional resistance for different water discharges (Text S2.2 in Supporting Information S1). We then subtracted the friction due to the smooth wall from the total frictional stress to find the stresses acting on the gravel bed and gravel bank. Weighting by the relative area of the bed and bank, we found values for the coefficient of friction for the gravel (Text S2.3 in Supporting Information S1). These data compared well to the Ferguson (2007) variable-power equation for shallow and rough flow,

$$C_{f,g} = \frac{a_1^2 + a_2^2 (H/k_{s,g})^{5/3}}{a_1^2 a_2^2 (H/k_{s,g})^2} \tag{14}$$

using the recommended non-dimensional constants of $a_1 = 6.5$ and $a_2 = 2.5$ with $k_{s,g} = 2.5D_{84}$ (Figure S2 in Supporting Information S1).

For the permafrost experiments, we followed the same procedure to isolate the frictional stress on the eroding permafrost bank. We used the 1-D backwater equation fit to find the total frictional stress in the test section (Text S3.1 in Supporting Information S1), subtracted off the stress components due to the smooth wall (Blasius, 1950) and the gravel bed (Equation 14), corrected for narrow channel hydraulics following Li et al. (2022), and solved for the remaining frictional stress on the eroding permafrost bank (Text S3.2 in Supporting Information S1). This coefficient of friction for the bank stress ($C_{f,b}$) represents both grain drag and any morphologic form drag (Lamb et al., 2008) from scallops that developed on the eroding bank (described in Text S3.2 in Supporting Information S1). To calculate the component due to grain drag ($C_{f,bg}$) on the sand bank, we followed the method of Wright and Parker (2004), solving the Colebrook-White equation (Colebrook, 1939; commonly displayed in the Moody diagram),

$$\frac{1}{\sqrt{8C_{f,bg}}} = -2.00 \log_{10}\left(\frac{2.51}{\mathrm{Re}\sqrt{8C_{f,bg}}} - \frac{k_s}{3.70H}\right), \tag{15}$$

with $k_{s,bg} = 3.5D_{84}$ and $u^*_{bg} = \sqrt{gH_{bg}S}$. We differenced the grain component from the total bank stress to find any remaining drag, which we assign to morphologic form drag ($C_{f,bm}$). We then needed to determine the appropriate roughness lengthscales ($k_{s,b}$ and $k_{s,bm}$) to substitute into Equation 12 and evaluate C_h for total and morphologic bank drag. To solve for the effective roughness lengthscale for total bank drag ($k_{s,b}$), we set $u^*_b = U\sqrt{C_{f,b}}$ and solved Equation 15, substituting H for H_{bg}, u^*_b for u^*_{bg}, and $k_{s,b}$ for $k_{s,bg}$. To solve for the roughness lengthscale for morphologic form drag ($k_{s,bm}$), we set $C_{f,bm}U^2 = \sqrt{gH_{bm}S}$ and solved for the flow depth attributed to morphologic drag (H_{bm}, m). We then solved Equation 15, substituting $u^*_m = U\sqrt{C_{f,bm}}$ for u^*_{bg}, H_{bm} for H_{bg}, and $k_{s,bm}$ for $k_{s,bg}$.

3.3. Comparing Experiments and Theory

We used our measurements of the bulk density of permafrost (ρ_b), its mass fraction of ice (f_{ice}), and its initial temperature (T_0) in the ablation-limited erosion theory (Equation 10). We assumed constant bulk densities of sediment ($\rho_s = 2{,}650$) and ice ($\rho_{\mathrm{ice}} = 920$ kg/m^3), latent heat of fusion of ice ($L_{f,\mathrm{ice}} = 333{,}550$ J/kg), fusion temperature ($T_f = 0$°C), and specific heat of sand ($c_{p,s} = 730$) and ice ($c_{p,\mathrm{ice}} = 2{,}093$ J/kg/°C). We used the average water flow velocity (U) and temperature (T_w) and assumed a constant water specific heat capacity ($c_{p,w} = 4{,}184$ J/kg/°C) and density ($\rho_w = 1{,}000$ kg/m^3).

We solved Equation 10 using four different values of the heat transfer coefficient, C_h. The first value used Equation 11 (Costard et al., 2003). The other three values used Equation 12 (Yaglom & Kader, 1974) with the wall drag parameterized as the total bank drag from the stress partitioning, the bank grain drag calculated from Equation 15, and the bank morphologic form drag that is the difference between total bank drag and bank grain drag. Our experiments had hydraulically transitional flow, with $\mathrm{Re}_{ks} \sim 90$ for the grain roughness lengthscale. To evaluate Equation 11, we inserted the flow depth (H) and the channel-averaged fluid flow velocity (U) to solve for the coefficient of heat transfer (C_h) assuming a constant Prandtl number ($\mathrm{Pr} = 10$, varies from 9 to 13 over the temperature range we investigated) and fluid kinematic viscosity ($\nu = 10^{-6}$ m/s^2). We used $A = 0.0078$, $\alpha = 0.3333$, and

$\beta = 0.9270$ (Lunardini, 1986), similar to the Costard et al. (2003) experiments. To solve Equation 12 for the three scenarios, we used $C_{f,b}$, u_b^*, and $k_{s,b}$ for the total bank drag; $C_{f,bg}$, u_{bg}^*, and $k_{s,bg}$ for bank grain drag; and $C_{f,bm}$, u_{bm}^*, and $k_{s,bm}$ for the bank morphologic drag.

4. Results

In this section, we first describe the stages that occurred during each experiment, using Experiment 1 as an example (Section 4.1). In Section 4.2, we evaluate the heat budget for the experiments. We then compare bank erosion rates from our experiments with theoretical rates calculated using heat transfer coefficients evaluated using the total bank friction and the bank friction due to grain and morphologic drag to understand the effects of bank roughness (Section 4.3). Finally, we compare the effects of changing water temperature, bank temperature, and bank ice content on modeled and experimental bank erosion rates (Section 4.4).

4.1. Experiment Progression

All frozen experiments proceeded through similar stages. Prior to the experiment (stage 0), we filled the channel to bankfull conditions. Experimental runtime was defined as the time since the start of stage 1. During stage 1, the channel remained at bankfull flow conditions as it widened and we increased the water discharge. At the end of the first stage, the frozen sand eroded back so that the channel was the same width as the gravel reaches (Figure 5c). The end of stage 1 had the highest quality data because there was a nearly constant width between the gravel reaches and the frozen reach, which minimized flow acceleration. In stage 2, water discharge was held constant as the bank continued to erode, such that the flow depth decreased in time as the channel widened. Stage 2 ended when sediment accumulated at the base of the eroding bank. We do not evaluate bank erosion theory for stage 2 because it experienced non-uniform and unsteady flow, which caused decreasing erosion rates due to declining bank and bed stresses.

Experiment 1 serves as an example case; processes were qualitatively similar in all experiments (Figures S4–S8 in Supporting Information S1; Movies S1, S2, S3, S4, and S5), but experiments with warmer water proceeded more rapidly (Table 2). In stage 0 of Experiment 1, there were near-normal flow conditions as we raised the water level, where the water surface slope in the test section was parallel to the channel bed. During the beginning of stage 1, the erodible-banked channel was narrower than the gravel-banked channel. This produced localized bank overtopping and undercutting by the flowing water at the upstream and downstream portions of the erodible bank. These reaches were not included in the test section analyzed for bank erosion rates because of their variable hydraulic conditions. The eroded sand was rapidly transported downstream as suspended load and the bank and bed did not accumulate any sediment. At the end of stage 1 ($t = 24$ min) the water experienced minimal spatial accelerations as the erodible sand bank and gravel sections had nearly equal widths. This marked the end of ablation-limited bank erosion conditions in Experiment 1, and afterward sand began accumulating at the toe of the bank.

Flow depth (Figure 6a) and water surface slope (Figure 6b) remained relatively constant throughout stage 1 of Experiment 1 as the channel widened because we increased water discharge (Figure 6c) to maintain near bankfull conditions. Discharge was increased in stage 0 at an irregular rate to fill the headbox and subsequently the channel with a low flow velocity. As the channel approached bankfull, we increased discharge to establish the water surface slope at $t = 3$ min. The bank was overtopped at $t = 3$ min, so we slightly decreased the discharge and kept it at a constant value until $t = 9$ min to avoid further overtopping. The discharge was then increased until $t = 24$ min and stage 1 ended. Water flow velocity remained relatively constant at 0.7 m/s through stage 1 (Figure 6d).

The sandy channel doubled in width during the experiment from less than 10 cm to over 20 cm, with nearly constant bank erosion rates in the latter part of stage 1 (Figure 6). The bank eroded back as a near vertical wall, maintaining a nearly rectangular cross-section with flow depths within 10% of 5.2 cm, which was nearly bankfull (bankfull depth was 5.6 cm). Shallow flow undercut the bank in stage 0, causing a delay between the start of water flowing through the experiment and erosion being recorded (Figure 6e). Once the water depth stabilized near bankfull (stage 1), erosion remained relatively constant, except for a brief peak in erosion rates 2 min into stage 1 when the undercut bank collapsed. The erosion rate decreased at the start of stage 2 when the discharge

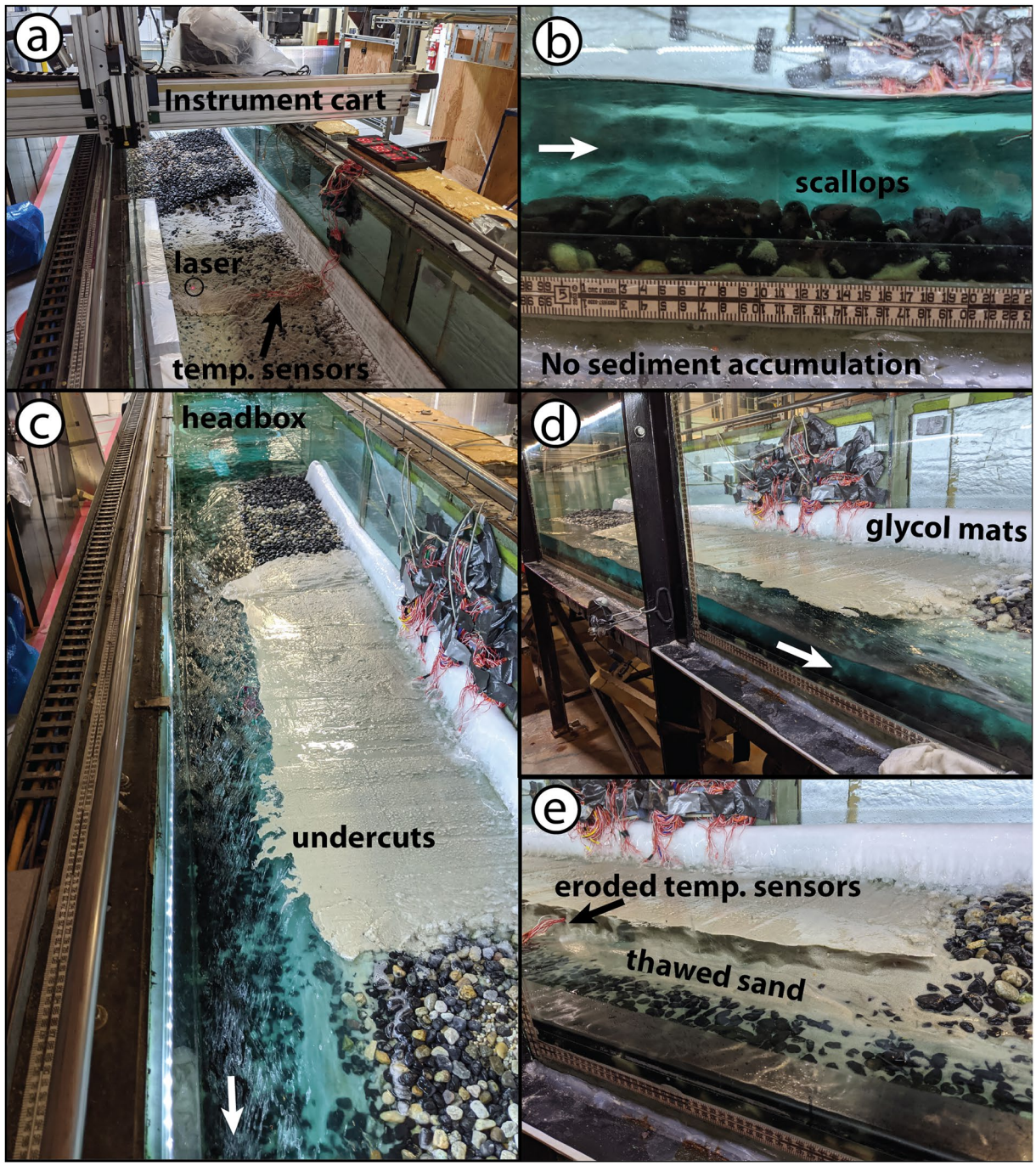

Figure 5. Setting up and running frozen bank Experiment 1, with water flow direction indicated by a white arrow. (a) Temperature sensors were laid out in an array using the Keyence laser on the instrument cart to set their position accurately. The bank was constructed of layers of frozen sand and ice with temperature sensors sandwiched between each layer, and the initial channel width was the thickness of the silver insulation mold to the left of the laser. (b) As water filled the channel, scallops rapidly formed on the bank. During this stage, all sediment was transported in suspension and did not accumulate on the gravel bed. (c) As the experiment progressed, the frozen bank eroded back until it was even with the immobile gravel in the test section. The upstream and downstream sections of the channel experienced unsteady water levels as the bank eroded, leading to undercuts that are cropped out during image processing steps. As the channel eroded, some thawed sand began to be deposited at the base of the bank and transported as bedload. (d) The downstream end of the bank continued to be undercut due to flow expansion, forming a thermoerosional niche just upstream of the gravel section. (e) After sand accumulated at the base of the eroding bank, we terminated the experiment and drained the channel and headbox, exposing the eroded temperature sensors, thawed sand, and scallops on the still-frozen bank.

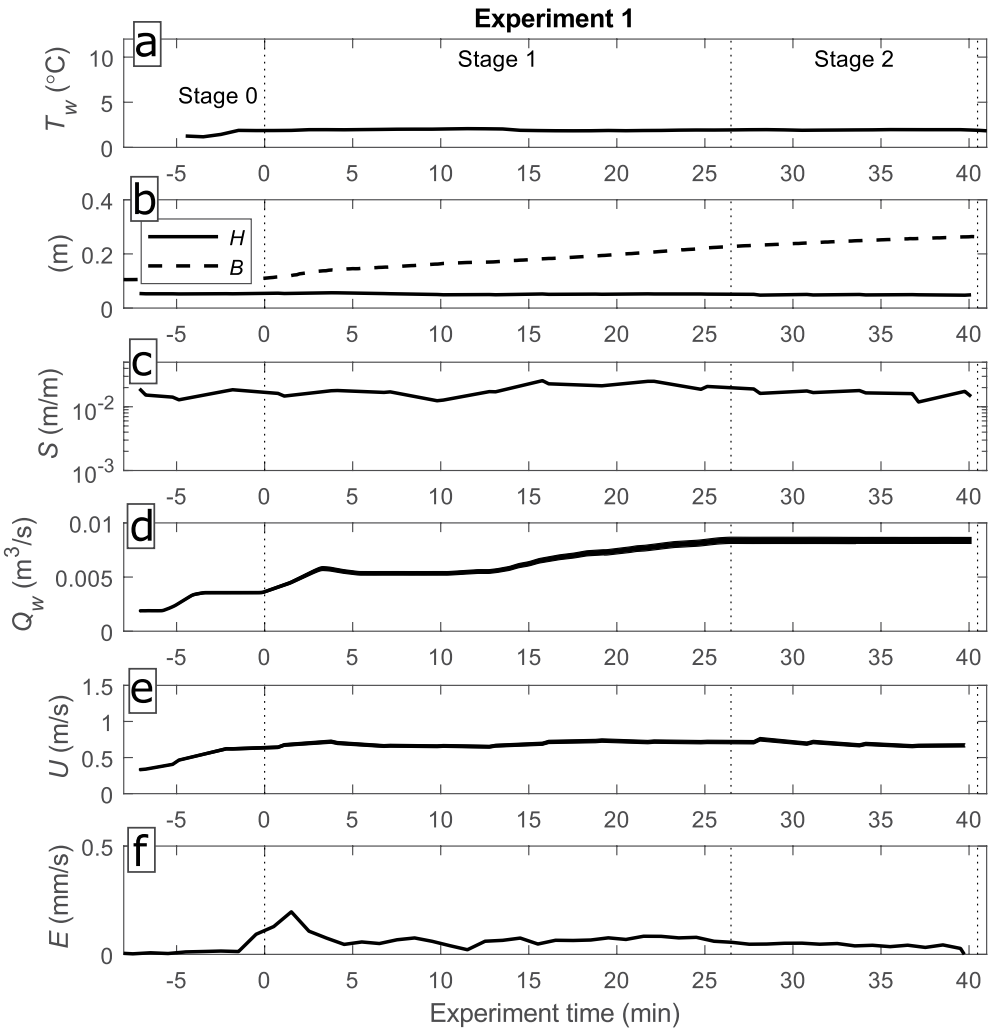

Figure 6. Measured and calculated thermal and hydraulic variables over the course of frozen flume Experiment 1. (a) Water depth (H) and channel width (B) measured in meters at $x = 22.5$ cm downstream using downstream Massa sonar scans. (b) Water surface slope (m/m) measured using a linear fit to water surface elevation from $x = 0$–70 cm downstream. (c) Water discharge (m^3/s) past the central temperature sensors. Discharge (Q_w) was measured using timelapse imagery at the channel inlet and corrected using the headbox dimensions and mean discharge velocity to the distance along the experimental bank. Line width includes 1 SD uncertainty in the discharge calibration. (d) Mean water flow velocity at the central temperature sensor array with line width enclosing 1 SD uncertainty. (e) Erosion rates were calculated by differencing the total bank area from 10-s timelapse images and averaging over a 1-min window.

reached its maximum value and the water surface slope began to drop, before erosion rates returned to zero when the experiment ended.

In all experiments, we observed features that mimicked thermoerosional niches observed in natural permafrost riverbanks (Figure 5b). Thermoerosional niches occur where frozen banks are undercut, forming ledges that extend meters (in the field) or centimeters (in our experiments) above the channel (Walker et al., 1987). In our experiments, they formed during stage 0 of the experiment and where the erodible bank meets the upstream and downstream gravel so the water level was lower than the top of the bank. During our experiments, we also observed erosional scallops ~5 cm long forming on the submerged bank. These appeared analogous to the scallops that form other on ice-fluid interfaces, such as in subglacial channels (Bushuk et al., 2019).

The temperature of the frozen bank varied throughout Experiment 1 (Figure 7). In general, temperature sensors closer to the surface of the bank were warmer since a thermal gradient developed between the glycol mats lining the channel bed and the warmer air. The average bank temperature increased over the course of the experiment due to heat fluxes from the flowing water and the warm air into the bank (q_a and q_c in Figure 7). By the end of the

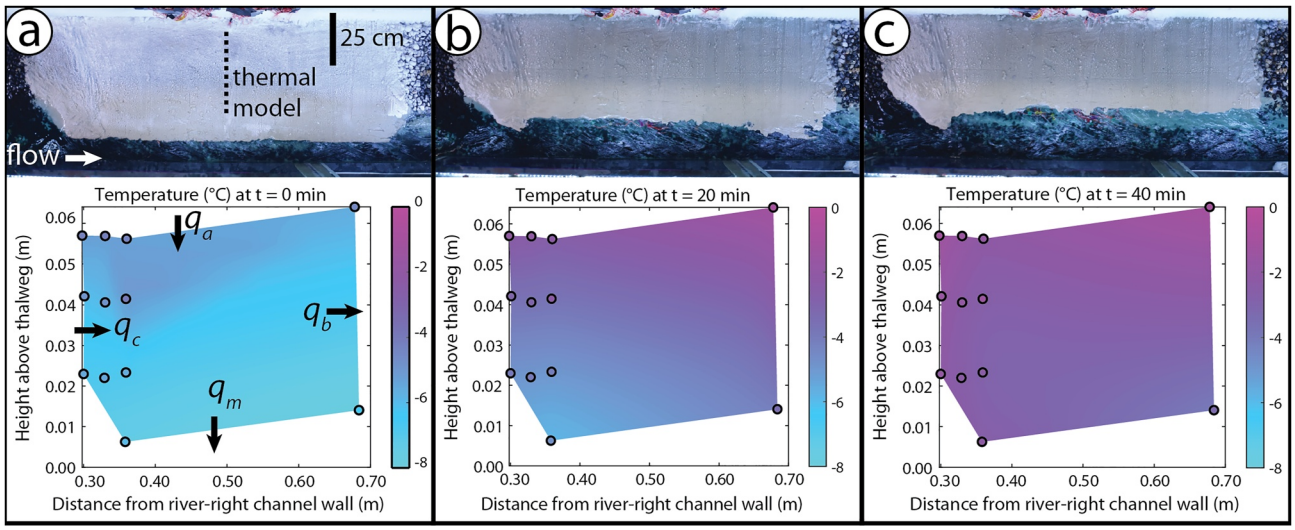

Figure 7. Overhead images and bank temperatures at the (a) start, (b) middle, and (c) end of Experiment 1. The overhead images have water flowing left to right. The lower panel shows the measurements from temperature sensors that did not erode in the experiment (circles) and a heat conduction model (shaded region). The heat conduction model was then used to calculate the heat fluxes from the air (q_a) and conducted into the un-eroded bank (q_c), glycol mats at the base of the bank (q_m), and the edge of the flume (q_b), as described in Section 4.2. We compared them to the latent heat of fusion (q_f) required to thaw the bank at observed erosion rates.

experiment, the bank temperature had increased from around −7°C to near 0°C, indicating that bank temperature in Experiment 1 was buffered by the latent heat of fusion.

4.2. Heat Budget

The theory for permafrost bank erosion presented in Section 2.1 is valid for a homogeneous bank with constant background temperature T_0, where the bank is eroding at a constant rate and its temperature profile has been established and translates uniformly at the same rate the bank is eroding (Randriamazaoro et al., 2007). These assumptions should be met when heat flow is primarily in 1-D, from the water into the bank material in the y-direction, without other sources of heat.

The assumption of homogeneous bank material was satisfied in our experiments, as the standard deviations were small for the bank bulk density and mass fraction of ice for each experiment (Table 2). In addition, we only analyzed data from the period during the experiments when erosion rates were roughly constant in time (stage 1), satisfying the constant rate constraint. Evaluating the 1-D heat flux assumption requires more consideration.

We fit a heat conduction model to the temperature sensor data at $x = 22.5$ cm far from the river channel to solve for the heat fluxes into the bank material. In particular, we solved for the heat flux from the air to the bank (q_a; J/m^2/s), from the frozen bank to the underlying glycol mats (q_m; J/m^2/s), from the frozen bank to the glycol mats where the bank is frozen to the flume wall (q_b; J/m^2/s), and conducted from the eroding bank (q_c; J/m^2/s) (Figure 8a). The conduction model solves the 2-D heat equation,

$$\rho_b c_{p,b} \frac{\partial T}{\partial t} - \nabla \cdot (\kappa_b \nabla T) = 0, \tag{16}$$

using Matlab's thermal PDE toolbox. The boundary conditions for temperature were set by the temperature sensor data (placed as the vertices of the control volume in the model domain) and the edges of the model domain were imposed using linear interpolation of temperature between the sensors (Figure 8a). We used measurements of f_{ice} to calculate $c_{p,b}$ (Equation 8). For saturated sediments, heat conduction occurs in parallel through sand and ice, producing a power-law relation for thermal conductivity of the frozen bank (κ_b; W/m/°C) (Farouki, 1981):

$$\kappa_b = \kappa_{\text{ice}}^{\lambda_p} \kappa_{\text{sed}}^{1-\lambda_p} \tag{17}$$

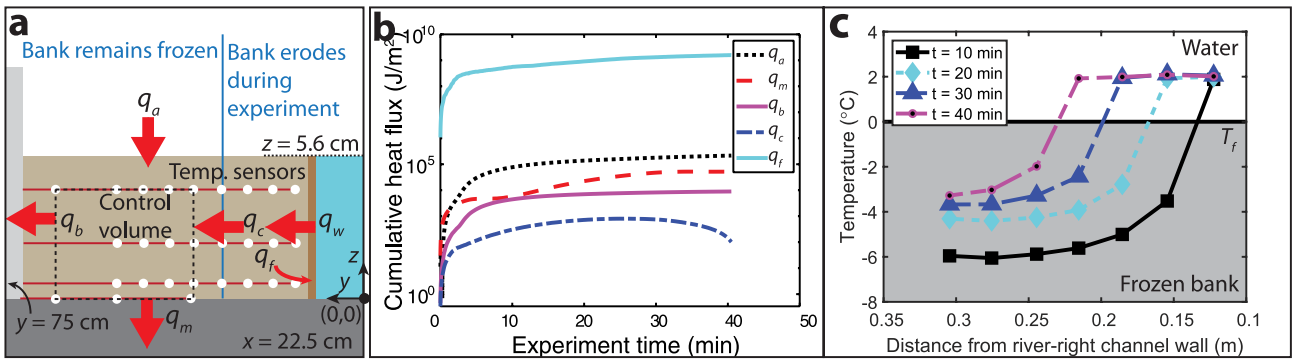

Figure 8. Cumulative heat fluxes in frozen region of the bank during Experiment 1. (a) Cartoon looking downstream of the heat conduction model control volume labeled with temperature sensors, y and z axes, and heat fluxes. Flux q_w is the heat flux to the bank, q_f is the heat of fusion required to thaw the bank at the observed erosion rates, q_a is the flux from the air to the top of the bank, q_c is the flux conducted past the thaw front and into the fixed control volume, q_b is the heat conducted to the mats on the side of the flume, and q_m is the flux conducted down into the gravel underlying the frozen bank. (b) The relative magnitude of cumulative heat fluxes throughout Experiment 1. (c) The bank temperature at 10, 20, 30, and 40 min into Experiment 1 for the line of sensors at $x = 22.5$ cm, $z \sim 3$ cm.

with the thermal conductivity of sediment of $\kappa_{sed} = 3.00$ W/m/°C (Powell et al., 1966), the thermal conductivity of ice of $\kappa_{ice} = 2.14$ W/m/°C (Bonales et al., 2017), and the bank volume fraction ice (λ_p; dimensionless). Bank volumetric porosity for saturated sediment is solved as follows:

$$\lambda_p = f_{ice}\rho_b/\rho_{ice}. \tag{18}$$

We compared modeled conductive heat fluxes to the heat flux required to thaw the eroded bank material,

$$q_f = EL_f\rho_b, \tag{19}$$

which provides a minimum bound on the heat flux from the flowing water to the bank, q_w, since $q_w = q_f + q_r$ and q_r equals the sum of q_c and the heat required to warm the bank material between the eroding bank and the heat conduction model domain (Figure 8a). This comparison showed that q_f was greater than q_a, q_c, q_b, and q_m by at least two orders of magnitude (Figure 8b; Figure S9 in Supporting Information S1), validating the assumption in Equation 10 that the heat balance is dominated by heat flux from the river water to the bank.

We also used the temperature sensors in the bank material to validate the ablation-limited bank erosion model assumptions that the temperature profile maintains a similar curvature over a conduction lengthscale δ and translates in the y-dimension in concert with the eroding bank. The temperature data for Experiment 1 (Figure 8c) shows that δ is approximately 0.1 m, and temperature ranges from a value near zero at the bank to a background value of T_0. The temperature gradient remains approximately constant in time, especially during stage 1 ($0 < t < 40{:}06$ for Experiment 1). Throughout the experiment, T_0 slightly increased due to warming of the bank material by the air, which accounts for deviation of the temperature profile from a purely 1-D Stefan solution. However, as constrained above, the heat flux from the air was negligible compared to the heat flux from the water to the bank (Figure 5b). Thus, we conclude that the experimental setup achieved a heat balance that was sufficiently 1-D and that the temperature profile translated in step with the eroding bank, such that the experiments should provide a robust test of Equation 10.

4.3. Bank Erosion Rates and Comparison to Theory

We compared our experimental measurements during stage 1 of the experiments to ablation-limited theory (Equation 10) using four different methods to calculate the coefficient of heat transfer (C_h): empirical fits from Costard et al. (2003) (Equation 11), the formulation of Yaglom and Kader (1974; Equation 12) using k_s and C_f calculated for the total bank friction, bank grain drag, and bank morphologic drag from scallops (see Section 3). Experimental measurements agree well with the ablation-limited erosion model (Equation 10) of permafrost riverbank erosion with C_h evaluated for rough banks using grain drag roughness (Figure 9a). Heat transfer coefficients calculated using bank morphologic and total drag predicted erosion rates significantly lower than those observed (Figures 9b and 9c). Measured erosion rates were significantly higher than erosion rates predicted using C_h from Equation 11 based on the closed pipe experiments (Costard et al., 2003; Lunardini, 1986) (Figure 9d).

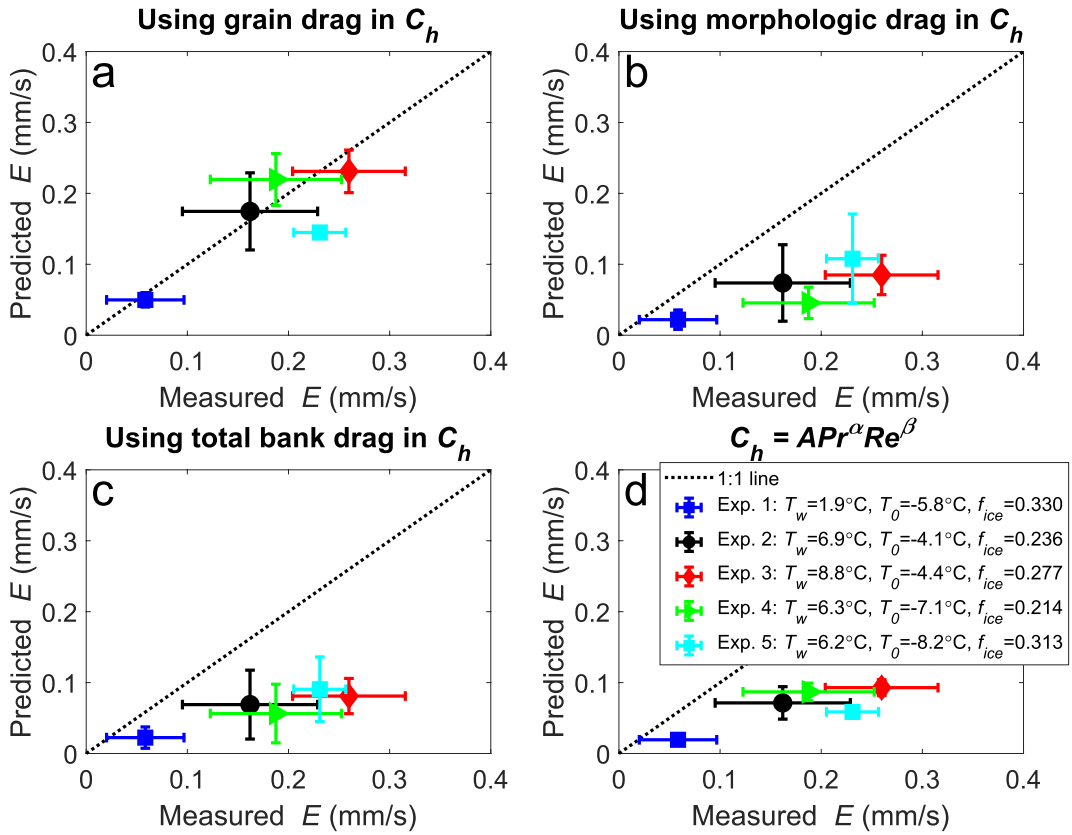

Figure 9. Comparison of experiments with modeled ablation-limited bank erosion rates calculated using heat transfer coefficients from (a) Equation 12 evaluated for bank grain roughness, (b) Equation 12 evaluated for bank morphologic roughness, (c) backwater modeling of total channel friction to evaluate total sand bank drag, and (d) Equation 11 using $A = 0.0078$, $\alpha = 0.3333$, and $\beta = 0.9270$. Error bars contain 1 SD of variability in measured and modeled erosion rates throughout each experiment.

In addition, the Yaglom and Kader (1974) heat transfer coefficient better captures the range of erosion rates seen in experiments, with 1 SD of modeled erosion rates scaling well with the variation observed in measured erosion rates. This implies that grain roughness significantly disrupts the diffusive sublayer and allows more rapid heat transfer to the frozen bank.

4.4. Effect of Water Temperature, Bank Temperature, and Pore Ice Content

Modeling bank erosion rates using Equation 10, the grain roughness lengthscale in Equation 12 best matches our experimental results (Figure 9a). Therefore, we compare the grain roughness bank erosion model to our data to isolate results on the effects of water temperature, bank temperature, and pore ice content.

Experiments 1–3 were designed to vary water temperature with all other parameters held approximately constant. To account for slight differences in conditions aside from water temperature between experiments and during the course of each experiment, we ran the erosion model for the measured thermal and hydraulic conditions as a function of time for each experiment. The shaded region represents the mean ± 1 SD for model results accounting for observed variations in all parameters except water temperature. Water temperature was a significant control on bank erosion rates, with warmer temperatures causing more rapid erosion (Figure 10a). Our observed erosion rates agree with calculated erosion rates (Equation 10) within 1SD when temporal variability in thermal and hydraulic conditions is accounted for. Results support that erosion rates scale linearly with the water temperature.

Experiments 3 and 4 were designed to vary bank temperature with all other parameters held approximately constant (Figure 10b). The temperature of the permafrost riverbank did not have a significant effect on measured erosion rates, despite varying nearly twofold (from −7 to −4.1°C) between Experiments 3 and 4. This spanned

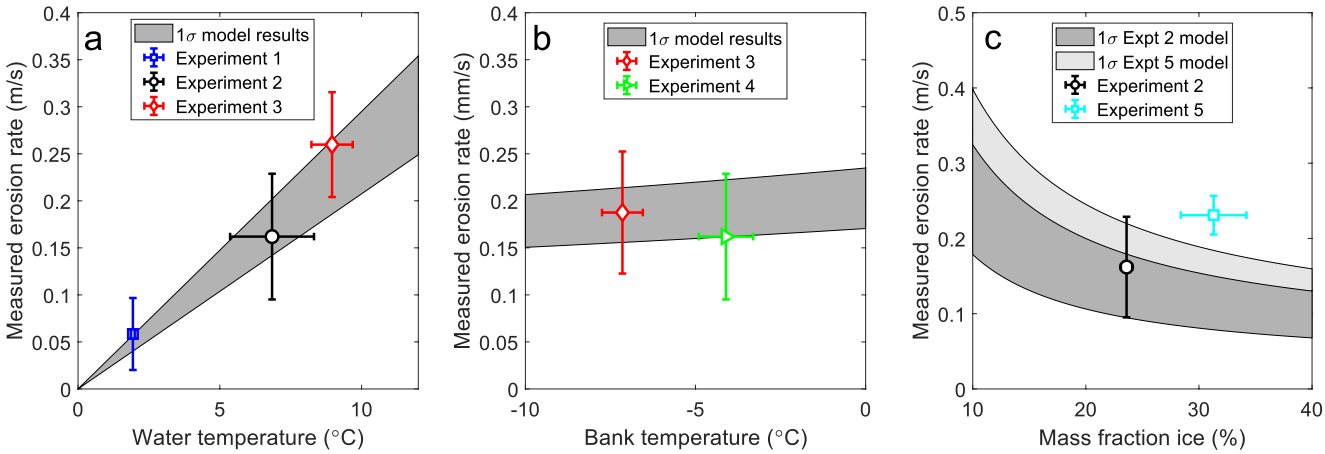

Figure 10. (a) Measured erosion rates versus water temperature for Experiments 1–3. The gray-shaded region encloses 1 SD of the Yaglom and Kader (1974) erosion rate model results calculated using grain drag for all three experiments, including variability in all parameters except water temperature. (b) Measured erosion rates versus bank ice content for Experiments 3 and 4, with the gray-shaded region enclosing 1 SD variability in the Yaglom and Kader (1974) grain drag erosion rate model results. (c) Measured erosion rates versus bank ice content for Experiments 2 and 5. The gray-shaded region encloses 1 SD of parameter variability for the Yaglom and Kader (1974) bank erosion model, with results calculated using grain drag, for each experiment.

the range of most natural permafrost terrain (Biskaborn et al., 2019), suggesting a negligible role in warming the bank material, compared to melting pore ice, in ablation-limited bank erosion. These results also support that q_a and q_m (Equation 1) can be neglected when comparing theory and our experiments (Figure 8).

Experiments 2 and 5 were designed to vary mass ice fraction with all other parameters held approximately constant (Figure 10c). Bank ice content ranged from 20.7 to 33.0 wt% (Table 2), and the difference in erosion rates between Experiments 2 and 5 can be explained by their difference in the mass fraction of ice. Slight differences in thermal and hydraulic conditions cause Experiment 5 to have higher modeled bank erosion rates than modeled erosion rates for Experiment 2 for the same ice content. Therefore, Experiment 5 has slightly higher erosion rates than Experiment 2, despite its bank containing 10 wt% less ice than the bank in Experiment 2. Both experiments agree with ablation-limited bank erosion theory, which indicates that higher ice content produces lower erosion rates with all else being equal.

5. Discussion

Our results indicate that the main driver of ablation-limited bank erosion in our experiments was water temperature. Previous experiments (Costard et al., 2003) and theory (Randriamazaoro et al., 2007) found that frozen bank erosion rates increased linearly with water temperature, in agreement with our results. Arctic river water temperatures are near 0°C for snow- and ice-melt, and river waters are subsequently warmed by heat transfer from the air (Blaen et al., 2013; Yang & Peterson, 2017; Zhilyaev & Fofonova, 2016). Arctic air temperatures are warming rapidly due to polar amplification (England et al., 2021), and corresponding increases in water temperature have been observed in many permafrost rivers (Docherty et al., 2019; Liu et al., 2005). Therefore, erosion rates, where set by pore-ice melting, should increase proportionally to air temperature as the Arctic warms.

The bank erosion model, heat conduction model, and experiments are in agreement that ablation-limited permafrost riverbank erosion is dominated by the phase change from ice to water rather than heating the bank material; the latent heat of fusion is orders of magnitude greater than the heat capacity of permafrost. Therefore, bank ice content is an important control on erosion rates (Dupeyrat et al., 2011), though our experiments and prior work did not address conditions when sediment is under-saturated (air is present in pore space), and it remains poorly understood whether these conditions can be modeled with existing theory. Our results also support the previous findings of Costard et al. (2003) in that erosion rates were little changed for experiments conducted over a 10°C difference in bank temperature (Figure 11).

To test the ablation-limited bank erosion theory, we took care to model thermal diffusion through the frozen bank and ensure that heat transfer was 1-D (Figure 7). We found that heat was transferred from the bank to the frozen ground across a lengthscale $\delta = 10$ cm. If this holds for field cases with banks comprising similarly well-sorted

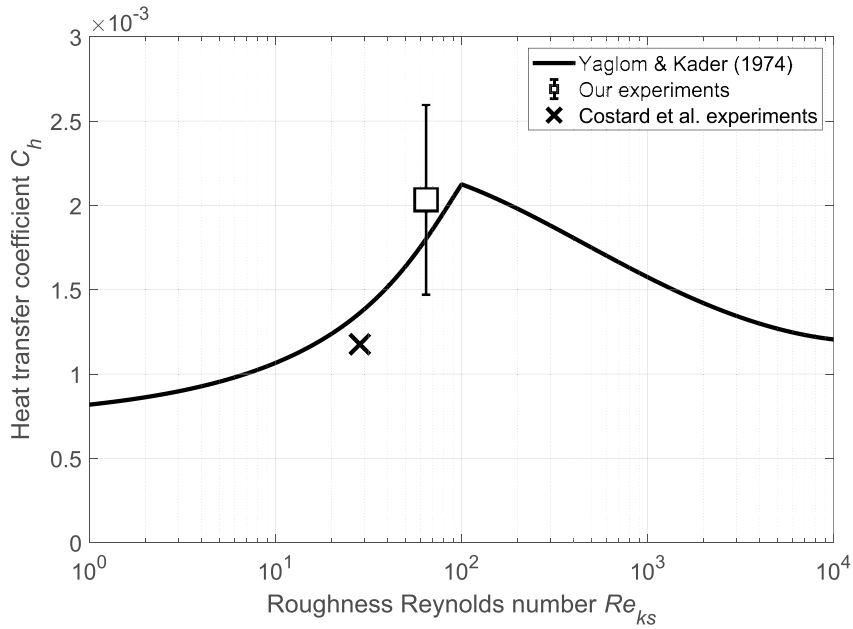

Figure 11. Heat transfer coefficient for fully turbulent flow (Equation 12), calculated for a range of k_s and $u*$ using empiricisms from Colebrook (1939) and Yaglom and Kader (1974). Our experiments show the mean and 1 SD error bars for C_h measured in Experiments 1–5. A representative value for the Costard et al. (2003) experiments is shown with Re_{ks} values for the sand ($k_s = 3.5(2.2D_{50})$, $H = 0.1$ m, $\mathrm{Re} = 1.5 \times 10^4$).

sand with pore ice, it implies that heat transfer is primarily in 1-D for natural riverbanks, unless the bank geometry is highly 3-D at the decimeter scale. In addition, we found that the heat flux from warm air on top of the bank was measurable but small during our experiments (Figure 7b). Most Arctic rivers are much deeper than our experiments (meter vs. cm-scale channel depths), which indicates that top-down seasonal thaw by warm air should not significantly alter permafrost bank erosion rates. Instead, we hypothesize that thaw by warm air may actually slow riverbank erosion at low water levels by thawing upper layers of the banks and causing slump block failure that subsequently insulates the submerged portion of the riverbank (e.g., Douglas, Dunne, & Lamb, 2023).

One unexpected result from our experiments was the development of scallops on the frozen bank. The scallops appear strikingly similar to ripples and scallops developed by water flowing past pure ice, which have been produced in the lab (Bushuk et al., 2019; Camporeale & Ridolfi, 2012) as well as observed migrating along the underside of river ice cover (Ashton & Kennedy, 1972). Although we did not observe the scallops migrating, they are known to grow and migrate in response to spatial patterns in flow turbulence (Bushuk et al., 2019), and they deserve further investigation on permafrost riverbanks in nature and in experiments.

Our results demonstrate that accurately accounting for bank roughness is important for predicting ablation-limited erosion of permafrost riverbanks. Using Equations 12 and 15, with all other variables kept constant, heat flux should increase with roughness in the hydrodynamically smooth and transitional flow regimes and decrease in the hydrodynamically rough flow regime, with a peak value near the transition (Figure 11). Heat transfer in the hydrodynamically smooth and transitional regimes increases with increasing bank roughness because sediment grains disrupt or thin the sublayer layer in which heat conduction is dominated by molecular diffusion, allowing for more efficient heat transfer (Figure 2b) (Yaglom & Kader, 1974). In the hydraulically rough regime, larger grains cause a decrease in rates of heat transfer because they cause flow separation, and heat transfer is relatively inefficient in turbulent wakes in the lee of grains (Yaglom & Kader, 1974). Our experiments had roughness Reynolds numbers that place them close to the theoretical peak in C_h. The rate of heat transfer in our experiments was higher by a factor of three compared to results from previous experiments (Costard et al., 2003; Randriamazaoro et al., 2007). Theory suggests that the greater heat transfer in our experiments compared to previous work can be attributed to the smoother walls in previous work (Figure 11).

Natural rivers contain a range of roughness scales, while the larger scales of roughness often dominate flow resistance (Darby et al., 2010; Kean & Smith, 2006a, 2006b), the peak in C_h at moderate Re_{ks} implies that

sand-size roughness may dominate heat transfer even if larger roughness forms are present. This appears to be the case in our experiments, which best matched heat-transfer theory using a grain-scale bank roughness despite the formation of larger scallops on the banks. In natural rivers, cohesive slump blocks and vegetation provide a similar source of morphologic bank drag that is larger than grain scale. While these large roughness elements may not influence heat transfer directly, they could indirectly slow thaw rates by slowing near-bank flow velocities. Further investigations, including using a near-bank flow velocity to calculate grain drag, are needed to better account for the multiple scales of roughness present on natural riverbanks.

The bank erosion rates in our experiments were much higher than is typical for natural rivers when averaged over many years (Rowland et al., 2019). For example, some of the highest reported permafrost riverbank erosion rates are along the Lena River (Costard et al., 2014): 2–40 m/yr, which occurred over a period of 6–39 days during ice break-up. Our slowest-eroding experiment (Experiment 1) produced erosion rates of 0.1 mm/s, or 52 m over a 6-day period and 340 m over a 39-day period. For a 4-month long open water season between ice break-up and freeze-up, continuous ablation-limited erosion would produce an unrealistic amount of bank erosion. Thus, a mechanism, different from pore-ice ablation, must limit bank erosion for large parts of the year (Douglas, Dunne, & Lamb, 2023). Such a limitation could come from sediment entrainment (Roux et al., 2017; Scott, 1978; Shur et al., 2021), the collapse of cohesive slump blocks (Barnhart et al., 2014; Parker et al., 2011), or root reinforcement of bank sediments (Ielpi et al., 2023). Our evaluation of the ablation-limited end member provides a foundation to disentangle the role of other erosion processes and develop a more complete model for long-term erosion rates in permafrost rivers.

6. Conclusions

Arctic rivers are experiencing increases in water temperature due to climate change that have the potential to thaw permafrost banks. In this study, we evaluated theory for ablation-limited riverbank erosion using flume experiments in which a frozen sand and ice mixture was exposed to erosion by a fully turbulent open-channel flow for a range of water temperatures, bank temperatures, and bank ice contents. Erosion rates were most sensitive to water temperatures showing a linear increase; they also increased with lower volumetric ice content and were relatively insensitive to bank temperature. Permafrost thaw is dictated in part by a heat transfer coefficient that describes the efficiency of heat transfer from the turbulent river to the bank. Using stress partitioning, we considered the effect of different scales of roughness of the eroding bank on heat transfer and found that a parameterization based on grain roughness best matched experimental results. Using the revised heat transfer coefficient, the experimental erosion rates were well-described by 1-D ablation-limited bank erosion theory. Thus, results support that where permafrost bank erosion is ablation-limited, erosion rates should increase with increasing river water temperature. However, ablation-limited theory predicts unrealistically high erosion rates when compared to seasonal averages, highlighting that additional processes beyond pore-ice thaw need to be incorporated to accurately model bank erosion rates in permafrost.

Data Availability Statement

Original photographs, laser topography scans, sonar measurements, discharge measurements, bank weight fraction water, grain size measurements, temperature sensor data, and instrument calibrations have been uploaded to a FAIR data repository (Douglas, Miller, et al., 2023).

Acknowledgments
The authors would like to thank Kieran Dunne, Grace Knuth, Maryn Sanders, Emily Geyman, Niccolo Ragno, Anya Leeman, and Sara Polanco for help running the experiments and Chris Paola and Todd Ehlers for fruitful discussions. This work was supported by NSF Awards 2127442 and 2031532, Caltech's Resnick Sustainability Institute, and the National Defense Science and Engineering Graduate Fellowship.

References

Alexander, M. T. (2008). *The influence of water content on the thermoerosion rate of frozen sand in moving water* (Master of Science). University of Alaska. Retrieved from https://www.proquest.com/openview/e6376000086472705b1b2e857adeba3f/1?pq-origsite=gscholar&cbl=18750

Ashton, G. D., & Kennedy, J. F. (1972). Ripples on underside of river ice covers. *Journal of the Hydraulics Division*, *98*(9), 1603–1624. https://doi.org/10.1061/JYCEAJ.0003407

Barnhart, K. R., Anderson, R. S., Overeem, I., Wobus, C., Clow, G. D., & Urban, F. E. (2014). Modeling erosion of ice-rich permafrost bluffs along the Alaskan Beaufort Sea coast. *Journal of Geophysical Research: Earth Surface*, *119*(5), 1155–1179. https://doi.org/10.1002/2013JF002845

Biskaborn, B. K., Smith, S. L., Noetzli, J., Matthes, H., Vieira, G., Streletskiy, D. A., et al. (2019). Permafrost is warming at a global scale. *Nature Communications*, *10*(1), 1–11. https://doi.org/10.1038/s41467-018-08240-4

Blaen, P. J., Hannah, D. M., Brown, L. E., & Milner, A. M. (2013). Water temperature dynamics in high Arctic river basins. *Hydrological Processes*, *27*(20), 2958–2972. https://doi.org/10.1002/hyp.9431

Blasius, H. (1950). The boundary layers in fluids with little friction (No. NACA-TM-1256). Retrieved from https://ntrs.nasa.gov/citations/20050028493

Bonales, L. J., Rodriguez, A. C., & Sanz, P. D. (2017). Thermal conductivity of ice prepared under different conditions. *International Journal of Food Properties*, *20*(sup1), 610–619. https://doi.org/10.1080/10942912.2017.1306551

Brabets, T. P., & Walvoord, M. A. (2009). Trends in streamflow in the Yukon River Basin from 1944 to 2005 and the influence of the Pacific Decadal Oscillation. *Journal of Hydrology*, *371*(1), 108–119. https://doi.org/10.1016/j.jhydrol.2009.03.018

Bronen, R., & Chapin, F. S. (2013). Adaptive governance and institutional strategies for climate-induced community relocations in Alaska. *Proceedings of the National Academy of Sciences of the United States of America*, *110*(23), 9320–9325. https://doi.org/10.1073/pnas.1210508110

Bushuk, M., Holland, D. M., Stanton, T. P., Stern, A., & Gray, C. (2019). Ice scallops: A laboratory investigation of the ice–water interface. *Journal of Fluid Mechanics*, *873*, 942–976. https://doi.org/10.1017/jfm.2019.398

Camporeale, C., & Ridolfi, L. (2012). Ice ripple formation at large Reynolds numbers. *Journal of Fluid Mechanics*, *694*, 225–251. https://doi.org/10.1017/jfm.2011.540

Colebrook, C. F. (1939). Turbulent flow in pipes, with particular reference to the transition region between the smooth and rough pipe laws. *Journal of the Institution of Civil Engineers*, *11*(4), 133–156. https://doi.org/10.1680/ijoti.1939.13150

Costard, F., Dupeyrat, L., Gautier, E., & Carey-Gailhardis, E. (2003). Fluvial thermal erosion investigations along a rapidly eroding river bank: Application to the Lena River (central Siberia). *Earth Surface Processes and Landforms*, *28*(12), 1349–1359. https://doi.org/10.1002/esp.592

Costard, F., Gautier, E., Fedorov, A., Konstantinov, P., & Dupeyrat, L. (2014). An assessment of the erosion potential of the fluvial thermal process during ice breakups of the Lena River (Siberia). *Permafrost and Periglacial Processes*, *25*(3), 162–171. https://doi.org/10.1002/ppp.1812

Darby, S. E., Trieu, H. Q., Carling, P. A., Sarkkula, J., Koponen, J., Kummu, M., et al. (2010). A physically based model to predict hydraulic erosion of fine-grained riverbanks: The role of form roughness in limiting erosion. *Journal of Geophysical Research*, *115*(F4), F04003. https://doi.org/10.1029/2010JF001708

Docherty, C. L., Dugdale, S. J., Milner, A. M., Abermann, J., Lund, M., & Hannah, D. M. (2019). Arctic river temperature dynamics in a changing climate. *River Research and Applications*, *35*(8), 1212–1227. https://doi.org/10.1002/rra.3537

Douglas, M., Miller, K. L., Schmeer, M., & Lamb, M. (2023). Supporting data for "Frozen flume experiments indicate rapid permafrost riverbank erosion depends on bank roughness" [Dataset]. US Department of Energy: Environmental System Science Data Infrastructure for a Virtual Ecosystem. https://doi.org/10.15485/1972218

Douglas, M. M., Dunne, K. B. J., & Lamb, M. P. (2023). Sediment entrainment and slump blocks limit permafrost riverbank erosion. *Geophysical Research Letters*, *50*(11), e2023GL102974. https://doi.org/10.1029/2023GL102974

Dupeyrat, L., Costard, F., Randriamazaoro, R., Gailhardis, E., Gautier, E., & Fedorov, A. (2011). Effects of ice content on the thermal erosion of permafrost: Implications for coastal and fluvial erosion. *Permafrost and Periglacial Processes*, *22*(2), 179–187. https://doi.org/10.1002/ppp.722

England, M. R., Eisenman, I., Lutsko, N. J., & Wagner, T. J. W. (2021). The recent emergence of Arctic amplification. *Geophysical Research Letters*, *48*(15), e2021GL094086. https://doi.org/10.1029/2021GL094086

Farouki, O. T. (1981). The thermal properties of soils in cold regions. *Cold Regions Science and Technology*, *5*(1), 67–75. https://doi.org/10.1016/0165-232X(81)90041-0

Ferguson, R. (2007). Flow resistance equations for gravel- and boulder-bed streams. *Water Resources Research*, *43*(5), W05427. https://doi.org/10.1029/2006WR005422

Gulley, J. D., Spellman, P. D., Covington, M. D., Martin, J. B., Benn, D. I., & Catania, G. (2014). Large values of hydraulic roughness in subglacial conduits during conduit enlargement: Implications for modeling conduit evolution. *Earth Surface Processes and Landforms*, *39*(3), 296–310. https://doi.org/10.1002/esp.3447

Hjort, J., Karjalainen, O., Aalto, J., Westermann, S., Romanovsky, V. E., Nelson, F. E., et al. (2018). Degrading permafrost puts Arctic infrastructure at risk by mid-century. *Nature Communications*, *9*(1), 5147. https://doi.org/10.1038/s41467-018-07557-4

Ielpi, A., Lapôtre, M. G. A., Finotello, A., & Roy-Léveillée, P. (2023). Large sinuous rivers are slowing down in a warming Arctic. *Nature Climate Change*, *13*(4), 1–7. https://doi.org/10.1038/s41558-023-01620-9

Isaksen, K., Romanovsky, V., Smith, S. L., & Drozdov, D. S. (2016). Thermal state of permafrost across the circumpolar permafrost regions–results from the latest assessment report, the SWIPA update. In F. Günther & A. Morgenstern (Eds.), *XI international conference on permafrost, book of abstracts* (pp. 444–445).

Kanevskiy, M., Shur, Y., Strauss, J., Jorgenson, T., Fortier, D., Stephani, E., & Vasiliev, A. (2016). Patterns and rates of riverbank erosion involving ice-rich permafrost (yedoma) in northern Alaska. *Geomorphology*, *253*, 370–384. https://doi.org/10.1016/j.geomorph.2015.10.023

Karjalainen, O., Aalto, J., Luoto, M., Westermann, S., Romanovsky, V. E., Nelson, F. E., et al. (2019). Circumpolar permafrost maps and geohazard indices for near-future infrastructure risk assessments. *Scientific Data*, *6*(1), 1–16. https://doi.org/10.1038/sdata.2019.37

Karlstrom, L., Gajjar, P., & Manga, M. (2013). Meander formation in supraglacial streams. *Journal of Geophysical Research: Earth Surface*, *118*(3), 1897–1907. https://doi.org/10.1002/jgrf.20135

Kean, J. W., & Smith, J. D. (2006a). Form drag in rivers due to small-scale natural topographic features: 1. Regular sequences. *Journal of Geophysical Research*, *111*(F4), F04009. https://doi.org/10.1029/2006JF000467

Kean, J. W., & Smith, J. D. (2006b). Form drag in rivers due to small-scale natural topographic features: 2. Irregular sequences. *Journal of Geophysical Research*, *111*(F4), F04010. https://doi.org/10.1029/2006JF000490

Kokelj, S. V., Lacelle, D., Lantz, T. C., Tunnicliffe, J., Malone, L., Clark, I. D., & Chin, K. S. (2013). Thawing of massive ground ice in mega slumps drives increases in stream sediment and solute flux across a range of watershed scales. *Journal of Geophysical Research: Earth Surface*, *118*(2), 681–692. https://doi.org/10.1002/jgrf.20063

Lamb, M. P., Dietrich, W. E., & Venditti, J. G. (2008). Is the critical Shields stress for incipient sediment motion dependent on channel-bed slope? *Journal of Geophysical Research*, *113*(F2), F02008. https://doi.org/10.1029/2007JF000831

Li, T., Venditti, J. G., Rennie, C. D., & Nelson, P. A. (2022). Bed and bank stress partitioning in bedrock rivers. *Journal of Geophysical Research: Earth Surface*, *127*(2), e2021JF006360. https://doi.org/10.1029/2021JF006360

Liu, B., Yang, D., Ye, B., & Berezovskaya, S. (2005). Long-term open-water season stream temperature variations and changes over Lena River Basin in Siberia. *Global and Planetary Change*, *48*(1), 96–111. https://doi.org/10.1016/j.gloplacha.2004.12.007

Lunardini, V. J. (1986). *Experimental determination of heat transfer coefficients in water flowing over a horizontal ice sheet* (CRREL Report No. 86–3). US Army Corps of Engineers, Cold Regions Research & Engineering Laboratory.

Maldonado, J. K., Shearer, C., Bronen, R., Peterson, K., & Lazrus, H. (2013). The impact of climate change on tribal communities in the US: Displacement, relocation, and human rights. *Climatic Change*, *120*(3), 601–614. https://doi.org/10.1007/s10584-013-0746-z

Malyarenko, A., Wells, A. J., Langhorne, P. J., Robinson, N. J., Williams, M. J. M., & Nicholls, K. W. (2020). A synthesis of thermodynamic ablation at ice–ocean interfaces from theory, observations and models. *Ocean Modelling*, *154*, 101692. https://doi.org/10.1016/j.ocemod.2020.101692

Miyake, Y., Tsujimoto, K., & Nakaji, M. (2001). Direct numerical simulation of rough-wall heat transfer in a turbulent channel flow. *International Journal of Heat and Fluid Flow*, *22*(3), 237–244. https://doi.org/10.1016/S0142-727X(01)00085-6

Nield, D. A., & Bejan, A. (2017). *Convection in porous media* (5th ed.), (Vol. 3). Springer International Publishing.

Obu, J. (2021). How much of the Earth's surface is underlain by permafrost? *Journal of Geophysical Research: Earth Surface*, *126*(5), e2021JF006123. https://doi.org/10.1029/2021JF006123

Obu, J., Westermann, S., Bartsch, A., Berdnikov, N., Christiansen, H. H., Dashtseren, A., et al. (2019). Northern Hemisphere permafrost map based on TTOP modelling for 2000–2016 at 1 km^2 scale. *Earth-Science Reviews*, *193*, 299–316. https://doi.org/10.1016/j.earscirev.2019.04.023

Parker, G., Shimizu, Y., Wilkerson, G. V., Eke, E. C., Abad, J. D., Lauer, J. W., et al. (2011). A new framework for modeling the migration of meandering rivers. *Earth Surface Processes and Landforms*, *36*(1), 70–86. https://doi.org/10.1002/esp.2113

Peterson, B. J., Holmes, R. M., McClelland, J. W., Vörösmarty, C. J., Lammers, R. B., Shiklomanov, A. I., et al. (2002). Increasing river discharge to the Arctic Ocean. *Science*, *298*(5601), 2171–2173. https://doi.org/10.1126/science.1077445

Pitlick, J., Marr, J., & Pizzuto, J. (2013). Width adjustment in experimental gravel-bed channels in response to overbank flows. *Journal of Geophysical Research: Earth Surface*, *118*(2), 553–570. https://doi.org/10.1002/jgrf.20059

Powell, R. W., Ho, C. Y., & Liley, P. E. (1966). *Thermal conductivity of selected materials* (National Standard Reference Data System No. 8). Thermophysical Properties Research Center, US Department of Commerce, National Bureau of Standards. Retrieved from https://nvlpubs.nist.gov/nistpubs/legacy/nsrds/nbsnsrds8.pdf

Randriamazaoro, R., Dupeyrat, L., Costard, F., & Gailhardis, E. C. (2007). Fluvial thermal erosion: Heat balance integral method. *Earth Surface Processes and Landforms*, *32*(12), 1828–1840. https://doi.org/10.1002/esp.1489

Roux, N., Costard, F., & Grenier, C. (2017). Laboratory and numerical simulation of the evolution of a river's talik. *Permafrost and Periglacial Processes*, *28*(2), 460–469. https://doi.org/10.1002/ppp.1929

Rowland, J., Stauffer, S., & Schwenk, J. (2019). Pan-arctic river bank erosion and accretion, and planform metrics measured over intervals ranging from 1973 to 2016. Incorporating the Hydrological Controls on Carbon Cycling in Floodplain Ecosystems into Earth System Models (ESMs). https://doi.org/10.15485/1571527

Scott, K. M. (1978). *Effects of permafrost on stream channel behavior in Arctic Alaska* (Geological Survey Professional Paper No. 1068) (p. 19). U.S. Geological Survey.

Shishkina, O., & Wagner, C. (2011). Modelling the influence of wall roughness on heat transfer in thermal convection. *Journal of Fluid Mechanics*, *686*, 568–582. https://doi.org/10.1017/jfm.2011.348

Shur, Y., Jones, B. M., Kanevskiy, M., Jorgenson, T., Jones, M. K. W., Fortier, D., et al. (2021). Fluvio-thermal erosion and thermal denudation in the yedoma region of northern Alaska: Revisiting the Itkillik River exposure. *Permafrost and Periglacial Processes*, *32*(2), 277–298. https://doi.org/10.1002/ppp.2105

UAF, & USACE. (2019). *Statewide threat assessment: Identification of threats from erosion, flooding, and thawing permafrost in remote Alaska communities* (No. INE 19.03) (p. 99). Denali Commission.

Vanoni, V. A., & Brooks, N. H. (1957). *Laboratory studies of the roughness and suspended load of alluvial streams* (Report or Paper No. 11) (p. 130). California Institute of Technology. Retrieved from https://resolver.caltech.edu/CaltechKHR:SedLabRpt-E-68

Walker, H. J., & Hudson, P. F. (2003). Hydrologic and geomorphic processes in the Colville River delta, Alaska. *Geomorphology*, *56*(3), 291–303. https://doi.org/10.1016/S0169-555X(03)00157-0

Walker, J., Arnborg, L., & Peippo, J. (1987). Riverbank erosion in the Colville Delta, Alaska. *Geografiska Annaler - Series A: Physical Geography*, *69*(1), 61–70. https://doi.org/10.1080/04353676.1987.11880197

Wright, S., & Parker, G. (2004). Flow resistance and suspended load in sand-bed rivers: Simplified stratification model. *Journal of Hydraulic Engineering*, *130*(8), 796–805. https://doi.org/10.1061/(ASCE)0733-9429(2004)130:8(796)

Yaglom, A. M., & Kader, B. A. (1974). Heat and mass transfer between a rough wall and turbulent fluid flow at high Reynolds and Peclet numbers. *Journal of Fluid Mechanics*, *62*(3), 601–623. https://doi.org/10.1017/S0022112074000838

Yang, D., & Peterson, A. (2017). River water temperature in relation to local air temperature in the Mackenzie and Yukon basins. *Arctic*, *70*(1), 47–58. https://doi.org/10.14430/arctic4627

Zhilyaev, S., & Fofonova, V. (2016). Numerical analysis and reconstruction of the temperature regime of the Lena River segment. In *2016 third international conference on mathematics and computers in sciences and in industry (MCSI)* (pp. 224–228). https://doi.org/10.1109/MCSI.2016.049

References From the Supporting Information

Blasius, H. (1913). Das aehnlichkeitsgesetz bei reibungsvorgängen in flüssigkeiten. In *Mitteilungen über forschungsarbeiten auf dem gebiete des ingenieurwesens: Insbesondere aus den laboratorien der technischen hochschulen* (pp. 1–41). Springer. https://doi.org/10.1007/978-3-662-02239-9_1

Einstein, H. A. (1950). *The bed-load function for sediment transportation in open channel flows*. US Government Printing Office.